Molecular Diversity (2021) 25:1905–1927
https://doi.org/10.1007/s11030-021-10188-5

ORIGINAL ARTICLE

# Molecular docking, binding mode analysis, molecular dynamics, and prediction of ADMET/toxicity properties of selective potential antiviral agents against SARS-CoV-2 main protease: an effort toward drug repurposing to combat COVID-19

**Himanshu Rai[1] · Atanu Barik[1] · Yash Pal Singh[1] · Akhil Suresh[2] · Lovejit Singh[1] · Gourav Singh[1] · Usha Yogendra Nayak[2,3] · Vikash Kumar Dubey[4] · Gyan Modi[1]**

Received: 2 November 2020 / Accepted: 19 January 2021 / Published online: 13 February 2021


## Abstract

The importance of the main protease ($M^{pro}$) enzyme of SARS-CoV-2 in the digestion of viral polyproteins introduces $M^{pro}$ as an attractive drug target for antiviral drug design. This study aims to carry out the molecular docking, molecular dynamics studies, and prediction of ADMET properties of selected potential antiviral molecules. The study provides an insight into biomolecular interactions to understand the inhibitory mechanism and the spatial orientation of the tested ligands and further, identification of key amino acid residues within the substrate-binding pocket that can be applied for structure-based drug design. In this regard, we carried out molecular docking studies of chloroquine (CQ), hydroxychloroquine (HCQ), remdesivir (RDV), GS441524, arbidol (ARB), and natural product glycyrrhizin (GA) using AutoDock 4.2 tool. To study the drug-receptor complex's stability, selected docking possesses were further subjected to molecular dynamics studies with Schrodinger software. The prediction of ADMET/toxicity properties was carried out on ADMET Prediction™. The docking studies suggested a potential role played by CYS145, HIS163, and GLU166 in the interaction of molecules within the active site of COVID-19 $M^{pro}$. In the docking studies, RDV and GA exhibited superiority in binding with the crystal structure of $M^{pro}$ over the other selected molecules in this study. Spatial orientations of the molecules at the active site of $M^{pro}$ exposed the significance of S1–S4 subsites and surrounding amino acid residues. Among GA and RDV, RDV showed better and stable interactions with the protein, which is the reason for the lesser RMSD values for RDV. Overall, the present *in silico* study indicated the direction to combat COVID-19 using FDA-approved drugs as promising agents, which do not need much toxicity studies and could also serve as starting points for lead optimization in drug discovery.

✉ Gyan Modi
gpmodi.phe@itbhu.ac.in

1 Room # 23, Department of Pharmaceutical Engineering and Technology, Indian Institute of Technology (Banaras Hindu University), Varanasi, Uttar Pradesh 221005, India

2 Department of Pharmaceutics, Manipal College of Pharmaceutical Sciences (MCOPS), Manipal Academy of Higher Education, Manipal, Karnataka 576104, India

3 Manipal McGill Centre for Infectious Diseases, Prasanna School of Public Health, Manipal Academy of Higher Education, Manipal, Karnataka 576104, India

4 School of Biochemical Engineering, Indian Institute of Technology (Banaras Hindu University), Varanasi, Uttar Pradesh 221005, India

**Graphic abstract**

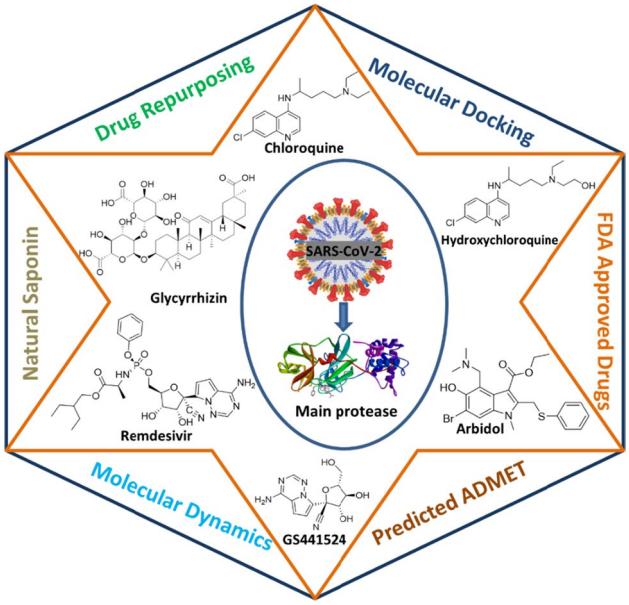


**Keywords** Molecular docking · Dynamics/simulation study · Potential antiviral agents · SARS-CoV-2 main protease ($M^{pro}$)

## Introduction

Coronavirus disease (COVID-19) is a newly emerged severe acute respiratory disease caused by the new coronavirus 2019-nCoV, later named SARS-CoV-2. The recent outbreak of COVID-19 first emerged in the seafood market of Wuhan city, Hubei province of China, in December 2019, which became a pandemic and created a global health emergency [1]. More than 210 countries have been affected due the disease's rapid transmission, with more than 26.9 million confirmed cases, and over eighteen million confirmed deaths worldwide [2]. The extremely contagious nature of SARS-CoV-2 and the rapid transmission of the virus between human to human through droplets or direct communication are major concerns for all sectors of society across the world [3]. Several efforts are ongoing to develop SARS-CoV-2 therapeutic agents and vaccines; however, only societal distancing is the best possible option so far, resulting in involuntary isolations/quarantines worldwide at different time points [4–8]. The severity of the COVID-19 outbreak could impose significant changes to health systems across the globe if the dissemination of the virus is not effectively controlled [9, 10].

The causative agent of this devastating disease, COVID-19 belongs to the beta coronavirus, which shares 89.1% nucleotide similarity with acute respiratory syndrome corona virus (SARS-CoV) [11]. COVID-19 is a single-stranded RNA virus containing 30,000 base pairs. The key amino acid residues are conserved in many viral key drug targets, including those found in both SARS-CoV and SARS-CoV-2 pathogens. Consequently, many common viral targets are structurally similar to SARS-CoV and likely to be inhibited by the same compounds. The emergence of COVID-19 has severely compromised the arsenal of antiviral and antibiotic drugs [12]. A plethora of literature evidence indicated the vital application of drug repurposing for various infectious diseases [13–15].

Currently, the specific therapeutic agent or antiviral compound for treatment against SARS-CoV-2 is still under investigation. Thus, to combat the rapid spread of SARS-CoV-2 disease, the identification of effective therapeutic agents is a major challenge for clinicians nowadays. The drug repurposing technique has emerged as a potential fast-track approach in recent years for speedup identification of therapeutic compounds for treatment against COVID-19, amongst other therapeutic agents that demonstrated broad-spectrum antiviral activity against SARS-CoV or MERS-CoV [16, 17]. The repurposing strategy has effectively identified potential therapeutic compounds against several highly contagious viral diseases such as Zika virus infection, Ebola virus-induced fever, and hepatitis C viral infection [18–21].

It has been shown in the literature that the FDA approved antimalarial and autoimmune disease drug chloroquine (**CQ**) and hydroxychloroquine (**HCQ**), known to inhibit viral infection by raising endosomal pH [22–25]. The antiviral drug remdesivir (**RDV**) and its active metabolites **GS441524**

can inhibit the growth of SARS-CoV-2 and are found to be efficacious in the clinic in combination [23, 26–28]. A commercially available broad-spectrum antiviral drug classified as a virus–host cell fusion inhibitor, arbidol (ARB, umifenovir), has entered into a clinical trial to treat COVID-19 [29, 30]. Interestingly, glycyrrhizin or glycyrrhizic acid or glycyrrhizinic acid (**GA**), a natural triterpene saponin, is active against coronaviruses [31]. The mechanism of action of these drugs is currently under investigation for the treatment of COVID-19. To determine the binding interaction of these ligands and the complexes' stability, we carried out the docking and molecular dynamics studies with these molecules with the SARS-CoV-2 main protease ($M^{pro}$; also called 3CLpro). The $M^{pro}$ enzyme of SARS-CoV-2 is one of the most attractive antiviral drug targets because of its highly conserved nature in coronaviruses, and the critical role player in the viral replication almost exclusively relies on the $M^{pro}$'s activity. $M^{pro}$ is the protein of interest because it plays a crucial role in polyprotein processing, which is translated from the viral RNA [32]. Apart from this, it is hypothesized that non-structural proteins (Nsp4-Nsp16), RNA-dependent RNA polymerase (RdRp; also known as Nsp12) as well as helicase (Nsp13) relay on $M^{pro}$ to get cleaved, which is essential for the maturation of virus [33]. We also carried out the *in silico* physicochemical properties prediction using ADMET Prediction™ (version 9.5, Simulation Plus, Lancaster, CA, USA) to cover a large range of drug-like properties and toxicities. The structures of these molecules are shown in Fig. 1. The *in silico* studies of these therapeutic targets were reported earlier with the hypothesis based on molecular mechanism aspects and ranking them on behalf of their best docking scores using O6K and N3 as a control agent [33]. However, the study is more focused on binding affinity score; therefore, the detailed interaction of these potential antivirals agents with $M^{pro}$ is still under investigation. Our purpose of performing this computational work with the selected ligands is to find out the detailed binding modes of these potential therapeutic candidates within $M^{pro}$ binding pocket, which could help to utilize these molecules as a template for the development of novel inhibitors and repurpose the other class of molecules.

## Material and methods

### Protocol for molecular docking studies

The *in silico* studies, viz. molecular docking, dynamics, and prediction of drug-like properties of the FDA-approved drugs CQ, HCQ, RDV, GS441524, ARB, and natural product GA (Fig. 1) were performed using SARS-CoV-2 main protease as the target protein.

The blind docking was carried out using the AutoDock 4.2 program package (http://autodock.scripps.edu/) [34]. The X-ray crystal structure of the SARS-CoV-2 $M^{pro}$ complex with a ∝-ketoamide inhibitor (PDB: 6Y2F, monoclinic form) was retrieved from the protein database (https://www.rcsb.org/) in.pdb format [17, 35]. The native co-crystal ligand O6K (inhibitor, 13b) was downloaded from the PDB database (https://pdbj.org/chemie/summary/O6K) in.pdb format to perform a docking validation study. The remaining ligands (CQ, HCQ, RDV, GS441524, ARB, and GA) were downloaded from the PubChem database in.sdf format (https://pubchem.ncbi.nlm.nih.gov/) and converted to.pdb file format by using Chem3D 15.0 software. Before moving for molecular

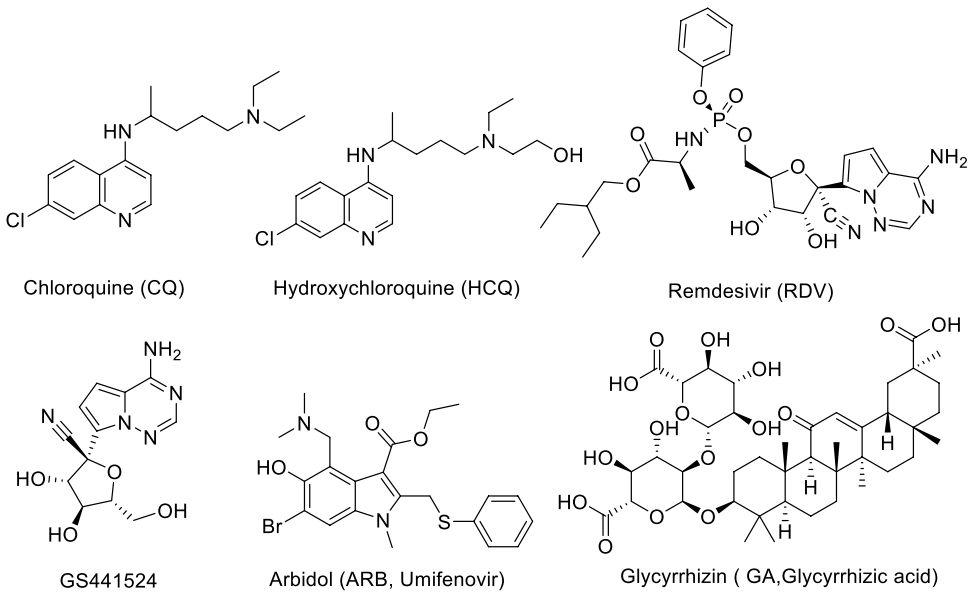


**Fig. 1** Chemical structures of the selected molecules for computational studies

docking, all the ligands' energy minimization was performed using an advanced molecule editor and visual tool, Avogadro [36]. For molecular docking, the receptor (protein) and ligand preparation were carried out using MGL and AutoDock tools, and output files were saved in.pdbqt formats. The post-dock receptor–ligand complex structures were analyzed for ligand–protein binding interaction using free Discovery Studio Visualizer for 2D and an immersive 3D visualization (Biovia, Discovery Studio Visualizer, Version 20.1.0.19295 Software; 2020).

The molecular docking studies and predictive binding energy estimation were carried out with a recently reported crystal structure of the $M^{pro}$ (PDB ID: 6Y2F) at resolution 1.95 Å. Flexible native co-crystal ligands were prepared using the protocol reported by Sarukhanyan et al. [37]. All the water molecules, co-crystal ligand, and heteroatoms were deleted from the protein.pdb files and subsequently added hydrogen atoms and Gasteiger charges to it using the MGL tool. Finally, the output file was saved in.pdbqt format. The ligands were energy minimized before converting them to a.pdbqt format. The grid box dimension was fixed at $55 \times 55 \times 54$ Å, at x, y, and z coordinates with 0.375 Å spacing, and the grid center (11.207, −1.02, and 20.757) was set corresponded to the centroid of the co-crystallized ligand structure (O6K). All the input files, including macromolecule and ligand.pdbqt files, grid parameter files (.gpf) and docking parameter files (.dpf), were generated using AutoDock graphical user interface. The genetic algorithm was used to evaluate parameters with the default setting, and Lamarckian GA (4.2) was employed for docking simulations. The Autogrid, AutoDock, and components of AutoDock tools were used to perform molecular docking and analyzed the best binding modes for receptor–ligand interactions. The lowest Gibbs free binding energy (estimated as ΔG in kcal/mol) conformers were selected for post-dock analysis. The same protocol was followed to perform molecular docking for the remaining ligands, namely CQ, HCQ, RDV, GS441524, ARB, and GA.

## Validation of AutoDock molecular docking

The docking procedure was followed the same as mentioned in the aforesaid protocol to re-docking the energy minimized ligand (O6K), and only the best-docked pose was superimposed to the crystal structure (PDB: 6Y2F) with a bound O6K molecule as a reference to calibrate the docking procedures. The binding interactions of the best-docked pose ($\Delta G = -7.40$ kcal/mol) correlated with the interactions that appeared in native reference co-crystal protein–ligand complex (PDB: 6Y2F) as shown in Fig. 2c.

## Molecular dynamics studies

Molecular dynamic studies were carried out using Schrödinger software on Maestro molecular modeling platform (Schrödinger Release 2019–4: Maestro, Schrödinger, LLC, New York, NY, 2019. version 12.2.012). The MD simulations were carried out on a workstation having Ubuntu platform, with Intel® Xenon(R) Gold 6130 CPU @ 2.10 GHz × 64 processors, Quadro P620/PCIe/SSE2 graphics card, and 134.8 GB RAM.

The binding stability and interaction profile of the docked complex of potent inhibitors GA and RDV were subjected to MD studies. For this study, a 30-nsec molecular dynamics simulation was performed using the Desmond module of Schrödinger [38]. The best docked posed as an output file from AutoDock was used as an input file to run MD. Solvation of the protein–ligand complex was performed using the TIP3P water model using the system builder tool of Desmond; an orthorhombic simulation box with a buffer distance of 10 Å between the box edge and atoms of the complex was generated. The system was neutralized by adding a suitable number of counter-ions, while the isosmotic condition was maintained by adding 0.15 M NaCl to the simulation box. The system was energy minimized with a maximum of 20,000 steps, and a modified relaxation protocol was applied for equilibration of the system as described in our previous publication. The MD simulation was performed at $300^0$ K at atmospheric pressure of 1.013 Bar. A total of 1000 frames were recorded and saved to the trajectory during the 30-nsec simulation. A simulation interaction diagram was used for the analysis of the trajectory obtained for the MD simulation.

## In silico prediction of physicochemical and ADMET properties

The different physicochemical and ADMET-related properties of all the compounds were predicted *in silico* using the trial version of software ADMET Prediction™ (version 9.5, Simulation Plus, Lancaster, CA, USA) and ChemDraw Professional 15.0 [39]. We used physicochemical and biopharmaceutical (PhysChem) and metabolism and toxicity modules to predict the *in silico* physicochemical properties. The ionization (*pKa*), lipophilicity, solubility, permeability, transporters, and pharmacokinetic parameters were predicted with the help of the PhysChem module. The various biotransformation-related properties, such as the possibility of being a substrate of CYP isoforms or UGT enzymes, potential to inhibit multiple drug-metabolizing enzymes, and enzyme kinetics parameters, were calculated by using the metabolism and toxicity module.

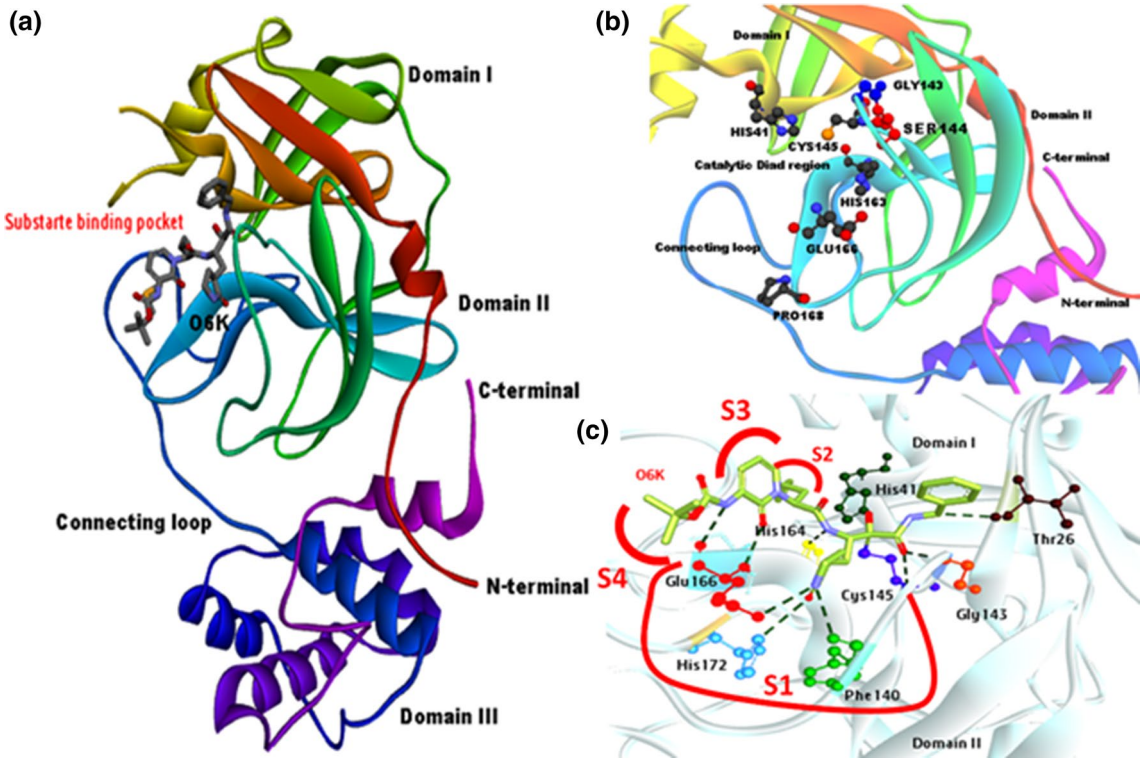


**Fig. 2** **a** Overview of co-crystallized O6K (Stick mode, color by elements) ligand In $M^{pro}$ catalytic domain (**PDB ID # 6Y2F**). **b** Close-up view of substrate binding pocket and molecular fragments (Ball and stick model, color by elements) of amino acid residues within the $M^{pro}$ substrate-binding cavity. **c** 3D interaction diagram of co-crystal ligand (O6K, stick mode, fluorescent green color, and color by molecule mode) with amino acid residues within $M^{pro}$ active site and representation of subsites S1 to S4 in substrate binding pocket

## Results and discussion

The crystal structure of SARS-CoV-2 $M^{pro}$ is a homodimer composite of two identical protomers, and each monomer is made up of three domains. The domains I (residues 8–101) and II (residues 102–184) forming a chymotrypsin fold and cleft between these domains serve as a substrate-binding pocket. Domain III (residues 201–303) is made up of five α-helices arranged in the form of a globular cluster, which regulates dimerization of proteins and is connected to domain II via a long extended loop region (residues 185–200) [40]. The C-terminal residues exist in the form of an extra domain. Active site residues located at the interface of domain I and domain II can be divided into subsites S1–S6, serving as a substrate-binding pocket for the binding of inhibitors as shown in Fig. 2a–c. The catalytic dyad His41–Cys145 is located at the S1 subsite. The S1 subsite's essential function involves the generation of an oxyanion hole when a conserved GLN carboxylate anion at the cleavage site interacts with CYS145, SER144, and GLY143, which can stabilize the transition process during proteolysis. The hydrophobic side chains are located at the S2 and S4 subsites (Fig. 2b–c).

### Binding interactions of potential antiviral agents at the active site of $M^{pro}$

In the present computational study, we have assessed the role of amino acids within the $M^{pro}$ active site for the selected target ligands in a well-versed optimized and validated docking protocol using co-crystal ligand (O6K) as a binding site reference standard (Fig. 2a). The optimized docking protocol was validated with positive control docking. The AutoDock tool was used to perform the redocking of the co-crystal ligand into the catalytic binding site of SARS-CoV-2 $M^{pro}$. The resultant conformer was found significantly overlapping with the co-crystal ligand (O6K) on superposition in the active pocket of $M^{pro}$. In addition, the root-mean-square deviation (RMSD) value between the docking and co-crystal ligand poses was determined using the PyMol application. The low RMSD value (< 0) validates the calibration of the docking protocol. To our information, such a systematic approach has not been applied earlier in the literature against SARS-CoV-2 main protease.

The overlay of docked O6K and co-crystallized O6K is shown in Fig. 3a. It demonstrates that the docking method works well because of the close agreement between the two poses of O6K. The γ-lactam moiety was found to be

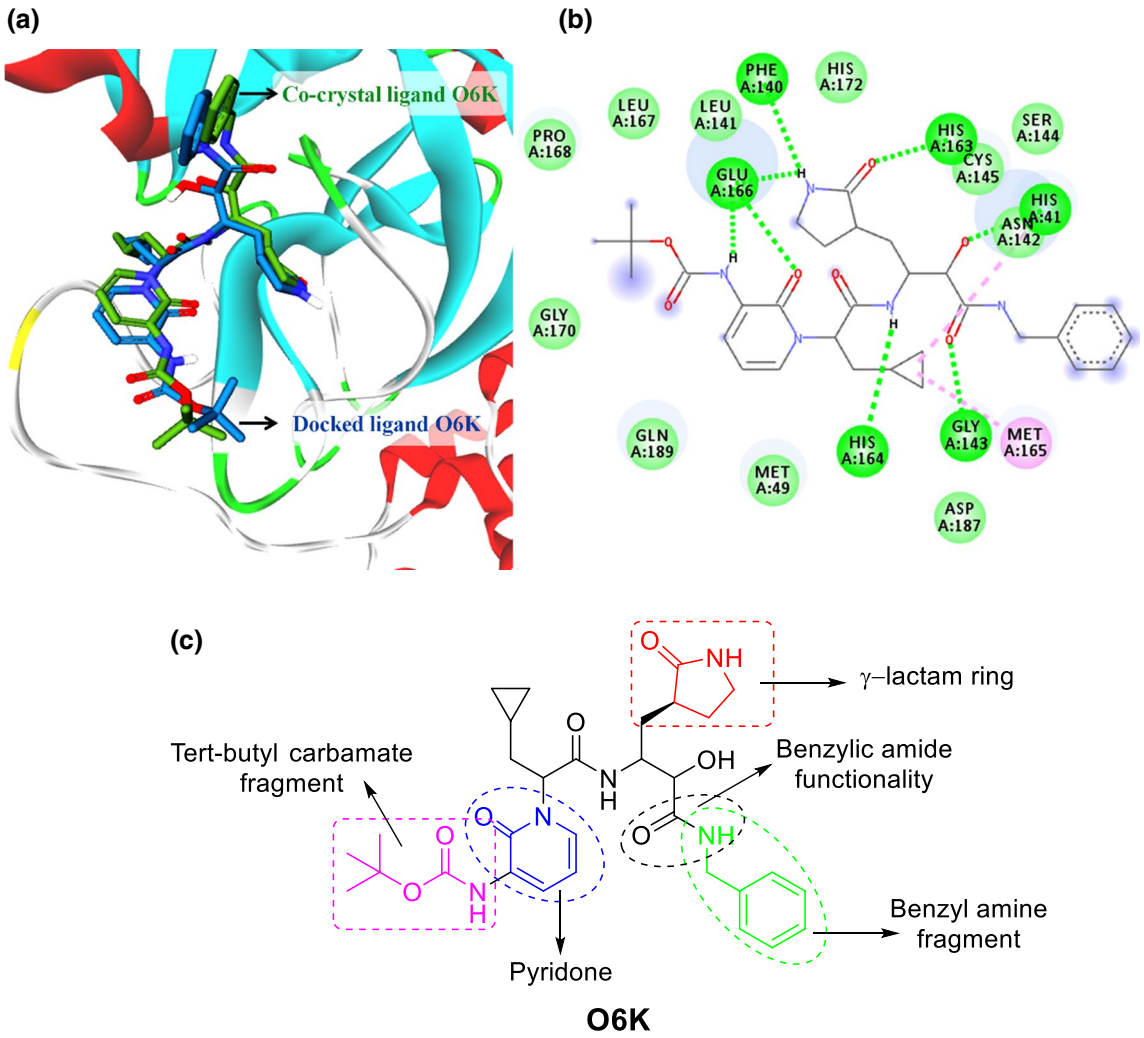


**Fig. 3** **a** Overlay of docked O6K and co-crystallized O6K (**PDB ID: 6Y2F**), hydrogen atoms were omitted for clarity. **b** 2D interaction diagram of O6K with amino acids of $M^{pro}$ cavity. **c** Representation of O6K with important functionalities

deeply embedded in the S1 pocket (Fig. 3b) of the protease and lactam nitrogen exhibited tri-center hydrogen bond interaction to the oxygen of PHE140 (2.55 Å) and with the carboxylate of GLU166 (2.47 Å). In comparison, carbonyl of lactam ring acts as hydrogen bond acceptor with the imidazole of HIS163 (1.85 Å, Fig. 3a). The carbonyl oxygen of the pyridone part of the inhibitor acts as a hydrogen bond acceptor with the amide of GLU166 (1.85 Å). The tert-butyl carbamate (Boc) amide acts as a hydrogen bond donor with the oxygen of GLU166 (1.74 Å). The carbonyl oxygen of benzylic amide showed hydrogen bonding with the amino group of GLY143 (2.63 Å). The carbonyl oxygen besides benzylic amide formed a hydrogen bond with the imidazole of HIS41 (2.83 Å). These favorable hydrogen bond interaction matches with reported interaction [32] showed the validation of docking protocol and respective residues' role in the catalytic domain responsible for the therapeutic agent's inhibitory activity.

The *in silico* study and binding mode analysis of CQ with $M^{pro}$ showed favorable three conventional hydrogen bond interactions, two alkyl hydrophobic interactions, and four mixed π-alkyl hydrophobic interactions at the active binding pocket, as shown in Fig. 4a. The quinoline nitrogen of CQ exhibited two hydrogen bond interactions with the terminal amino group (amidic) of GLN192 (2.16 Å) and with the amino group of THR190 (2.70 Å). The amino group, located at the fourth position, displayed favorable hydrogen bond interaction with the carbonyl oxygen group of GLU166 (1.73 Å). Interestingly, a carbon–hydrogen bond interaction was observed between the α-C of linear pentane carbon spacer and the carbonyl oxygen of HIS164 (3.60 Å). Apart from these, the chlorine atom at the seventh position of

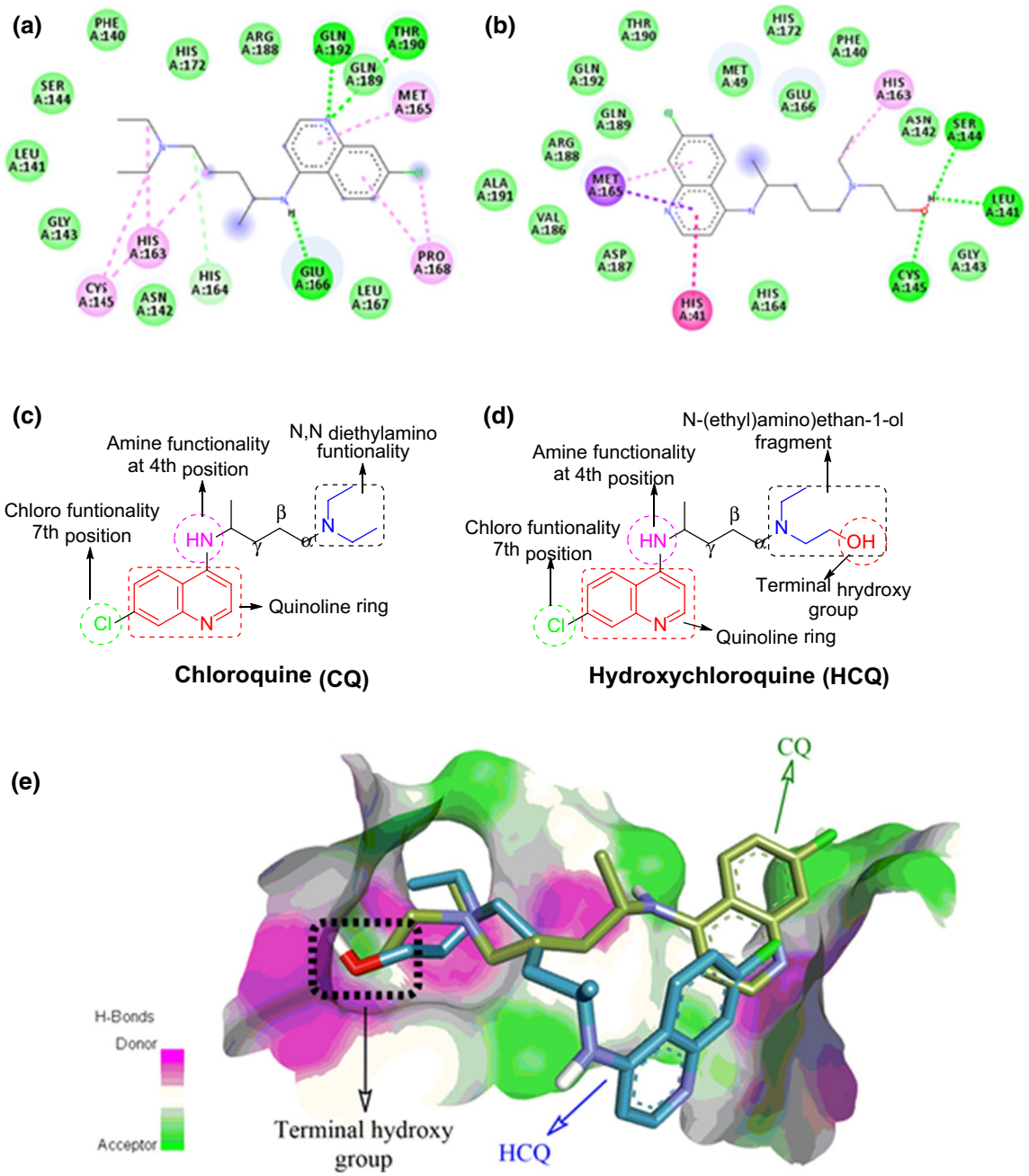


**Fig. 4** **a** 2D interaction diagram of CQ with amino acid residues of $M^{pro}$ cavity. **b** 2D interaction diagram of HCQ with amino acids of $M^{pro}$ cavity. **c**, **d** Chemical structures of CQ and HCQ with important functionality. **e** 3D surface representation of the ligand-binding pocket with the superimposed CQ-HCQ (conformers with the lowest docking score; CQ in green and HCQ in navy blue; ligands displayed in stick mode) and an annotation indicating the difference between the CQ and the HCQ ligand

the quinoline ring has an alkyl hydrophobic interaction with PRO168 (3.87 Å). The β-C of pentane carbon spacer and N, N diethyl-substituted carbon exhibited alkyl hydrophobic interactions with CYS145 (5.46 and 4.81 Å, respectively). Mixed π-alkyl hydrophobic interactions were observed for quinoline aromatic rings with M165 (4.52 Å) and PRO168 (5.15 Å). The terminal N, N diethylamino group also exhibited additional mixed π-alkyl hydrophobic interaction with HIS163 (4.29 Å). Similar interactions of antiviral drugs with $M^{pro}$ have been earlier reported in the literature [41]. The CQ exhibited a promising docking score value of − 6.41 kcal/mole (Table 1), which corroborates ligand stability at the interaction site and indicates a binding affinity for $M^{pro}$.

In the case of HCQ, the hydroxyl group of SER144 (2.94 Å), carbonyl oxygen of LEU141 (2.05 Å), and the amino group of CYS145 (2.31 Å) could make favorable

**Table 1** Binding free energy and interacting amino acids of selected therapeutic drugs with SARS-CoV-2 $M^{pro}$ (PDB ID # 6Y2F)

| Target ID | SARS-CoV-2 $M^{pro}$ (PDB ID # 6Y2F) | |
|---|---|---|
| | Binding free energy (kcal/mol) | Interacting amino acids |
| O6K | − 7.40 | GLU166 PHE140 HIS163 GLY143 HIS164 HIS41 MET165 |
| CQ | − 6.41 | GLN192 THR190 GLU166 HIS163 PRO168 MET165 CYS145 |
| HCQ | − 6.01 | SER144 LEU141 CYS145 MET165 HIS163 HIS41 |
| RDV | − 7.12 | CYS145 GLU166 GLN192 THR190 HIS41 PRO168 |
| GS441524 | − 5.66 | GLU166 GLN192 THR190 GLN189 PRO168 |
| ARB | − 7.0 | CYS145 HIS164 HIS41 HIS163 GLU166 PRO168 LEU167 |
| GA | − 8.21 | GLU166 PHE140 SER144 GLN189 CYS145 MET49 MET165 PRO168 |

conventional hydrogen bond interactions with the terminal hydroxyl group of the HCQ (Fig. 4b). Intriguingly, no conventional hydrogen bond interactions were observed with quinoline ring nitrogen to the active site amino acid residues, which we observed in the case of CQ. The quinoline ring of HCQ displayed a π-sigma hydrophobic interaction with MET165 (3.90/4.22 Å) and π–π interactions with HIS41 (4.84 Å). The ethyl substituted at the terminal nitrogen group exhibited π-alkyl hydrophobic interaction with HIS163 (5.27 Å). The affinity score of HCQ is -6.01 kcal/mole (Table 1), which also supports ligand stability at the interaction site and indicates a binding affinity for $M^{pro}$.

We found that both RDV and its metabolite (GS-441524) could form a complex with the Mpro with affinity scores of − 7.12 and − 5.66 kcal/mol, respectively. The docking and binding mode analysis of RDV showed that 3-hydroxy of furan ring has two hydrogen bond interactions with the amino group (amidic) of GLN192 (1.81 Å) and the carbonyl oxygen of carboxylic acid group of THR190 (2.06 Å, Fig. 5a). The hydroxyl oxygen at the fourth position of the furan ring formed conventional hydrogen bond interaction with the carbonyl oxygen of the carboxylic acid of THR190 (1.87 Å). The phosphoryl amino group of RDV displayed a conventional hydrogen bond interaction with the carbonyl oxygen of the carboxylic acid of GLU166 (1.73 Å). Interestingly, a carbon–hydrogen bond was observed between the carbon of methoxy substitution at the second position of the furan ring and the carbonyl oxygen of the carboxylic acid group of GLU166 (3.01 Å). The phenoxy aromatic ring at the phosphoryl group exhibited π-alkyl hydrophobic interaction with HIS41 (4.83 Å). The pyrrole ring of RDV made π-alkyl hydrophobic interaction with PRO168 (4.63 Å). A desirable binding free energy − 7.12 kcal/ mole (Table 1) comparable to O6K indicates favorable interaction of RDV with $M^{pro}$ and supports clinical efficacy as a potential inhibitor against SARS-CoV-2 infection.

The binding of GS441524 against $M^{pro}$ was accompanied by an affinity score of − 5.66 kcal/ mole with six favorable conventional hydrogen bond interactions at the viral protease's active binding site. The hydroxyl group at the third position on the oxolane ring could form hydrogen bond interaction with the amino group (amidic) of GLN189 (3.02 Å) and accept hydrogen bonding with the carbonyl oxygen of carboxylic acid of THR190 (2.07 Å, Fig. 5b). The fourth position hydroxyl group of oxolane ring displayed two hydrogen-bonding interactions with the amino group and with the carbonyl oxygen of acidic group of THR190 (1.68 and 1.99 Å, respectively), as well as additional hydrogen bonding to the amino group (amidic) of GLN192 (2.15 Å). The hydroxyl group of methoxy substitution at the fifth position of the oxolane ring similarly showed hydrogen bonding with the carbonyl oxygen of the carboxylic acid group of GLU166 (1.86 Å). A favorable π-lone pair interaction was observed between the carbonyl oxygen of the carboxylic acid group of GLU166 (2.96 Å) and the triazine ring of the GS441524. The intramolecular hydrogen bond interaction was observed between the hydroxyl group of methoxy substitution at the fifth position of oxolane ring and nitrogen at the 2nd position of triazine ring (1.92 Å) of GS441524. The pyrrole ring of GS441524 has π-alkyl hydrophobic interaction with PRO168 (4.65 Å).

Similar to RDV, the docking of ARB against the $M^{pro}$ showed comparable negative free energy − 7.0 kcal/ mole, as shown in Table 1. The N, N-dimethyl aminomethyl group at fourth position of the indole nucleus exhibited conventional hydrogen bond interaction with the carbonyl oxygen of carboxylic acid of HIS164 (2.11 Å), an unfavorable + ve/ + ve cationic (charge repulsion) interaction of nitrogen (amino group) with imidazole ring nitrogen of HIS41 (4.26 Å) and π-sigma hydrophobic interaction between the N-methyl and imidazole ring of HIS41 (4.25 Å, Fig. 6a). The hydroxyl group at the fifth position of the indole nucleus interacted favorably through hydrogen bonding with the carbonyl oxygen of the carboxylic acid group of HIS164 (1.81 Å) and with the sulfur group of CYS145 (2.60 Å). The bromo group at the sixth position of the indole nucleus displayed alkyl hydrophobic interaction with HIS163 (5.04 Å) and CYS145 (4.68 Å). The phenylthio substitution at the second position of the indole nucleus exhibited π-alkyl hydrophobic interaction with LEU167 (4.63 Å) and π-sigma hydrophobic

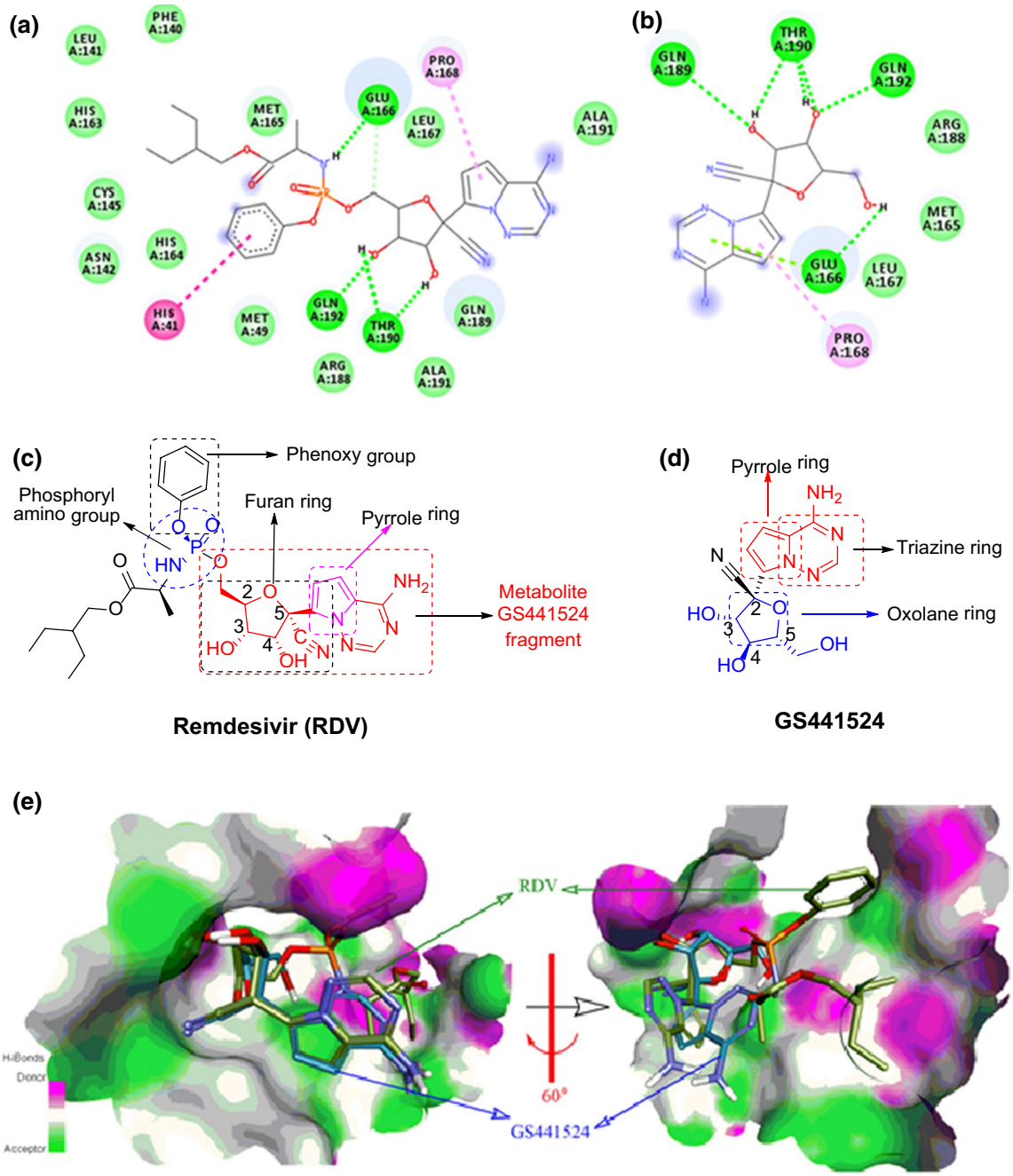


**Fig. 5** **a** 2D interaction diagram of RDV with amino acids of $M^{pro}$ active site. **b** 2D interaction diagram of GS441524 with amino acids of $M^{pro}$ active site. **c**, **d** Chemical structures of RDV and GS441524 with important functionality (fragments) labeled and shown in different colors. **e** 3D surface representation of the ligand-binding pocket with the superimposed RDV (green) -GS441524 (navy blue) and ligands are shown in stick mode)

interaction with PRO168 (4.63 Å). The indole nucleus displayed two π-donor hydrogen bond interactions with the amino group of GLU166 (2.55 and 3.77 Å) and one π-sulfur interaction with CYS145 (5.75 Å).

The AutoDock study of GA against the $M^{pro}$ revealed that the hydroxyl group at the fourth position of β-D-glucopyranuronosyl residue exhibited conventional hydrogen bond interaction with the carboxylate of GLU166 (2.06 Å, Fig. 6b). The hydroxyl group at the fifth position of α-D-glucopyranuronosyl residue made favorable hydrogen bonding with the carbonyl oxygen of carboxylic acid of PHE140 (1.91 Å) and formed a hydrogen bonding with the carbonyl oxygen of carboxylic acid at the sixth position with the hydroxyl group of SER144 (2.76 Å).

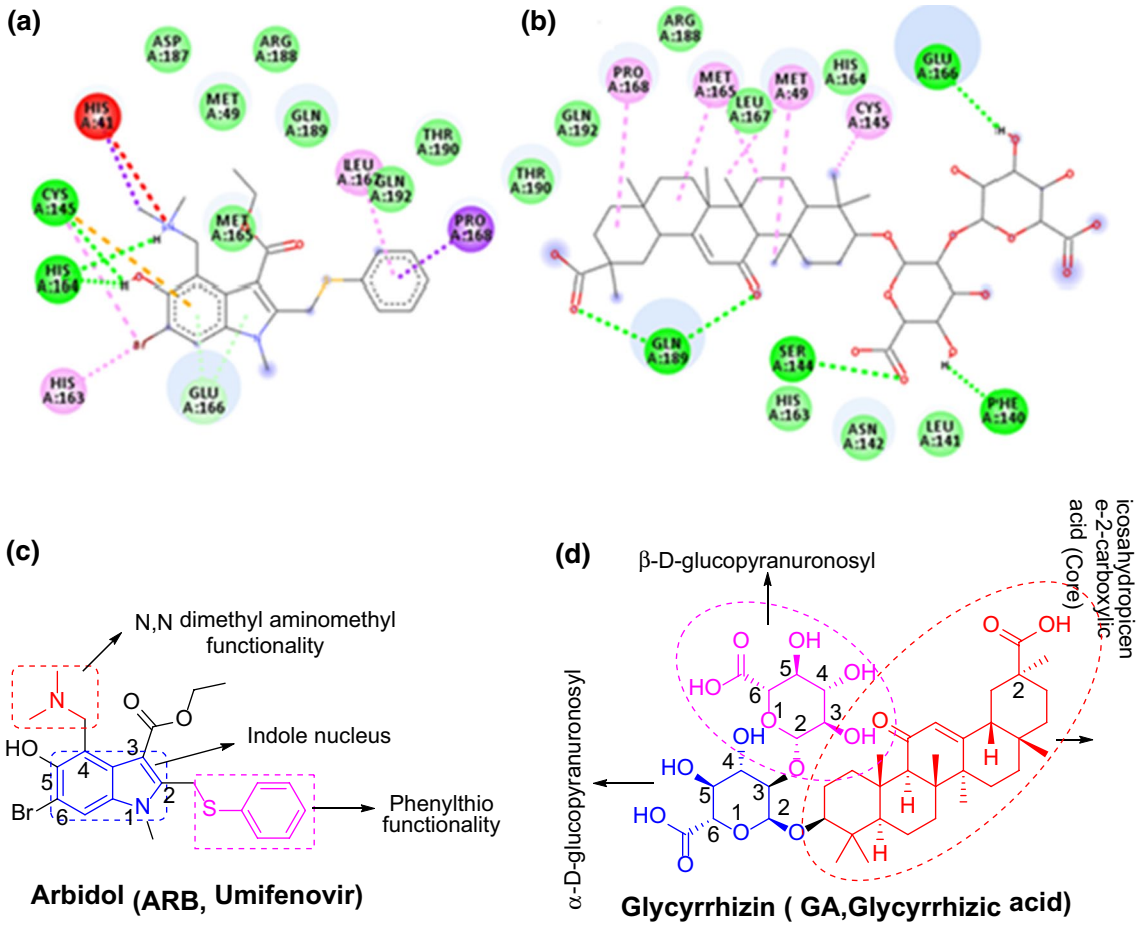


**Fig. 6** **a** 2D interaction diagram of ARB with amino acids of $M^{pro}$ active site. **b** 2D interaction diagram of GA with amino acids of $M^{pro}$ active site. **c**, **d** Chemical structures of ARB and GA with important functionality (fragments) are shown in different colors

The oxo group at the 14th position and the carbonyl oxygen of carboxylic acid at the second position of icosahydropicene-2-carboxylic acid core nucleus of GA exhibited conventional hydrogen bond interactions with the amino group of GLN189 (3.01 and 2.19 Å, respectively). Further, hydrophobic alkyl interactions were observed between the icosahydropicene-2-carboxylic acid core nucleus methyl groups of GA with CYS145 (4.48 Å), MET49 (4.94 and 4.99 Å), MET165 (4.62 and 5.03 Å), and PRO168 (4.88 Å). The GA exhibited the highest negative free energy of − 8.21 kcal/ mole (Table 1) among the selected therapeutic drugs, making it a promising therapeutic agent for the treatment of novel Cov-19 infection. Intriguingly, the unfavorable characteristic with violation of three, in terms of ' 'Lipinski's rule of five, the druggability of GA requires further investigational exploration using *in vitro* and *in vivo* testing to evaluate clinical efficacy as well as safety profile. This study provides preliminary observations on behalf of computational work. Therefore, wet-lab experiments are still the principal approach to evaluate and validate docking studies.

Several literature evidences are implicating that SARS-CoV-2 $M^{pro}$ could be used for screening purposes to predict the binding affinity of the approved drugs, natural inhibitors, and those in clinical trials [5, 42–44]. The binding stability of an α-ketoamide inhibitor O6K or 13b as reference control inside the SARS-CoV-2 $M^{pro}$ was carried out to assess affinity score and determine theoretically the possible and probable active site residues involved in the formation of complex, which was found consistent with our observation [44–47]. The Cys145-His41 catalytic dyad and amino acid residues CYS145, SER144, and GLY143 (collectively referred to as catalytic center), which are involved in the creation of an oxyanion hole, are essential for stabilizing the transition process during proteolysis [48]. It is reported that two hydrogen-bonding interactions with the catalytic center (S1 subsite) of the target proteases are advantageous, rather than only one [32]. The role of GLU 166 is considered to be critical for the dimerization of two protomers and contributes to the shaping of S1 pocket of the substrate-binding site [49]. All the ligands exhibited common amino acid interactions, particularly either CYS145 and/or HIS41 residues

of the active pocket's catalytic domain except GS441524 (exhibiting least binding affinity score), which indicates the critical role of these amino acids for inducing $M^{pro}$ inhibitory activity. Most of the ligands (O6K, RDV, ARB, and GA) with higher affinity score (> 7.0 kcal/mol) also exhibited a favorable hydrogen bond interaction with GLU166 within the active pocket, which in turn corroborates the role of GLU for instigating $M^{pro}$ inhibitory activity. The other favorable amino acid interactions are HIS163, and PRO168 seems to play a vital role in most of the ligands within the $M^{pro}$ active pocket. Recently in 2020, Nguyen et al. [50] also unveiled the fact that Gly143, Cys145, Glu166, and His163 of $M^{pro}$ are the region to form a hydrogen bond and highly favorable molecular fragments for the development of novel SARS-CoV-2 main protease inhibitors, which resembles the finding in the current study. *An in silico* study performed by Srivastava et al. demonstrates the binding stability of Glycyrrhiza glabra derivatives, i.e., GA as bioactive inhibitor inside the SARS-CoV-2 $M^{pro}$ and proposed HIS41, GLY143, GLN189, GLU166, CYS145, THR25, ASN142, MET49, and PRO168 present in the active site of $M^{pro}$ were shown to make non-covalent interaction with the target compound, which was found consistent with our observation [51].

In the present research, our objective is to predict active site residues of SARS-CoV-2 Mpro using clinically effective drugs via computational approaches in the site-specific SARS-CoV-2 Mpro catalytic domain, which is yet unknown. To our best knowledge, such binding mode interactions and molecular fragments (amino acid residues) of the $M^{pro}$ binding pocket are not reported so far. The docking score was found to be similar for O6K, whereas comparable in the case of RDV and ARB (− 7.12 kcal/mol and − 7.0 kcal/mol, respectively), and significantly different in the case of GS441524, CQ, HCQ (− 5.66 kcal/mol, − 6.41 kcal/mol and − 6.01 kcal/mol, respectively) as per the literature [33]. Our purpose of performing the computational work for these ligands is to visualize the complex interaction mode of these potential candidates within in $M^{pro}$ binding pocket, which could help us use these molecules as a template for the development of novel inhibitors. We assume that these interactions could help us understand the role of interacting amino acids within the active pocket site responsible for imparting the inhibitory potency and serve as a guiding tool in designing novel candidates with higher selective and potency against SARS-CoV-2 in the imminent future.

## Spatial orientations of clinically oriented molecules at the active site of $M^{pro}$

The γ-lactam ring of O6K drug molecule embedded in the catalytic dyad (HIS41-CYS145) domain is classified as S1 subsite. The cyclopropyl and tert-butyl group (Boc) of O6K arrange itself in a hydrophobic pocket coined as S2 and S4 subsites, respectively. The pyridone ring of O6K is embedded in the space surrounded by MET49 and GLN189, coined as S3 subsite within the active binding pocket of the viral $M^{pro}$ (Fig. 7a). To determine the spatial orientation of selected drugs within the active site of viral $M^{pro}$, an overlay of the best-docked pose of all the drugs was carried out with the complex of O6K-$M^{pro}$. From the superimposed image, it was observed that the quinoline ring of the CQ occupies the space between S3 and S4 subsites with chloro-group oriented away from the S4 subsite (Fig. 7b). The linear pentane chain of 4-amino group oriented itself toward the S1 subsite and terminal N,N-diethylamino group had hydrophobic interactions with HIS163 and CYS145 of the catalytic domain. A similar spatial orientation was observed in the case of HCQ (Fig. 7c). In the case of RDV, the 2-ethylbutyl ester attached to phosphorylamino group oriented toward the S1 subsite, while phenoxy group attached to it is embedded in the S2 subsite of the active binding pocket. The phosphorylamino group, along with tetrahydrofuran ring and pyrrolo[2,1-f4[1,2,48triazin-4-amine core nucleus, run parallel from subsite S3 to S4 in the described fashion within the active site of the $M^{pro}$ (Fig. 7d). However, in the case of its active metabolite of RDV, the same orientation for tetrahydrofuran ring and pyrrolo[2,1-f] [1, 2, 4]triazin-4-amine core nucleus was observed with GS441524, but no interaction with S1 subsite was observed, which could be a possible reason for the lower binding energy of GS441524 with $M^{pro}$ compared to other therapeutic drugs (Fig. 7e). The indole nucleus of ARB occupies the space at the center in between S1, S2, and S3 subsites. The bromo group at sixth position facing toward S1 subsite and N, N dimethylamino group at fourth position embedded in the S2 subsite of active binding site domain (Fig. 7f). The carboxylate group at the third position of the indole nucleus occupies the space of the S3 subsite, while phenylsulfanyl group at the second position of indole nucleus occupies the space in the hydrophobic S4 pocket of the active site in $M^{pro}$. The GA spatial orientation showed that the whole molecule aligns in a flipped C-shape from within the substrate-binding cleft of viral protease. The β-D-glucopyranuronosyl residue occupies the space of S4 subsite, and α-D-glucopyranuronosyl residue filled the space of S1 subsite (Fig. 7g). The icosahydropicene-2-carboxylic acid core nucleus of the GA is arranged alongside the backbone of the main chain within the S2 and S3 subsites of the substrate-binding cleft in viral protease.

To design the lead molecules, not only the structural templates from the existing therapeutic candidates (inhibitors) and molecular fragments (amino acid residues) of target protein, but the spatial orientations of biologically active targets inside the binding pocket are of considerable significance. These spatial orientations can help us to evaluate the role of different functionalities of a particular target and their arrangement within the binding pocket,

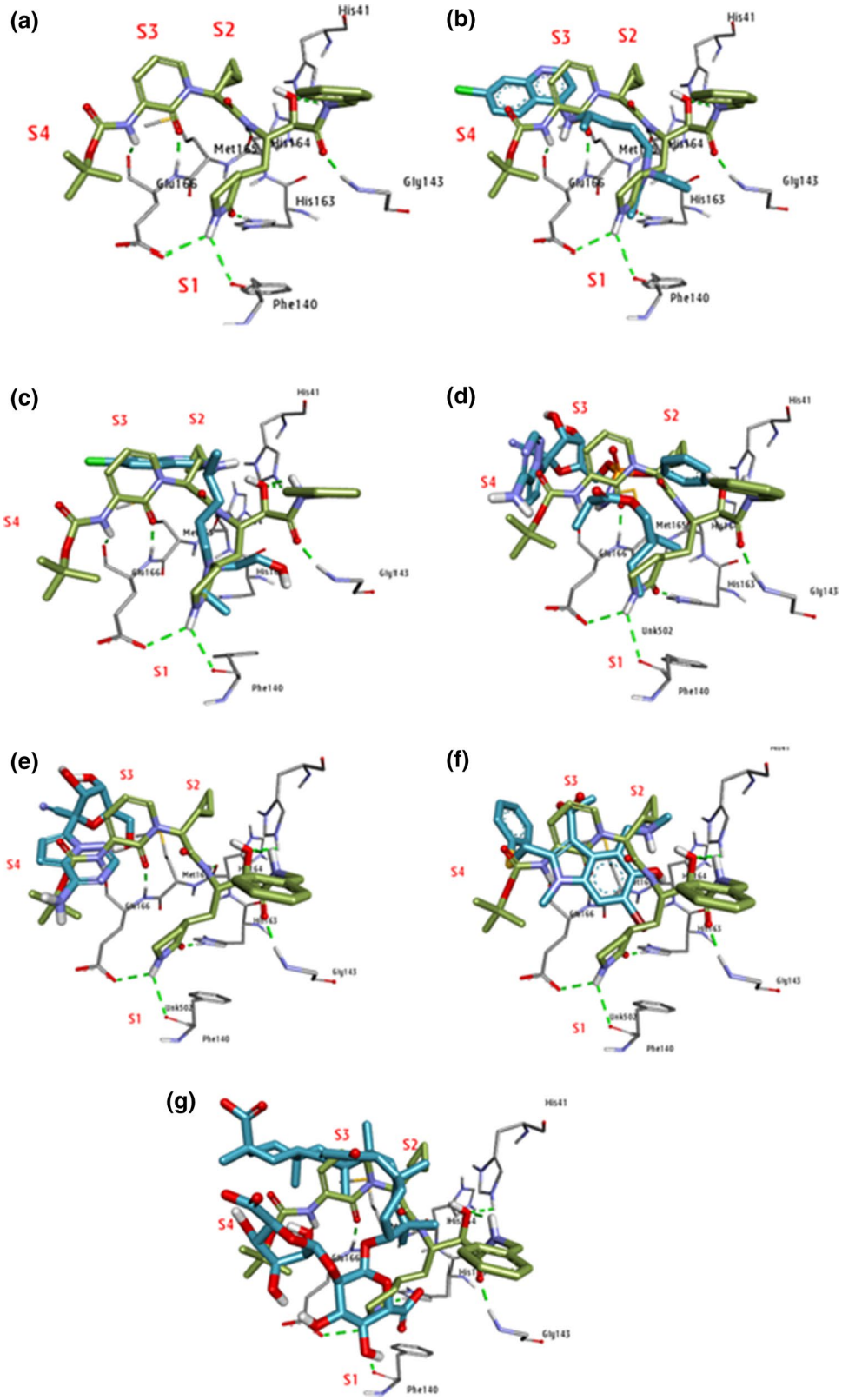


**Fig. 7** 3D-interaction diagram and spatial orientation of reference compounds 13b (O6K) and selected therapeutic drugs (CQ, HCQ, RDV, GS441524, ARB, and GA) in the substrate-binding cleft located between I and II domains of the $M^{pro}$, in the monoclinic crystal form. Image **a** the spatial orientation of re-docked reference ligand (O6K, green, stick mode) in the substrate-binding pocket of the viral $M^{pro}$. Images **b**–**g** overlay of CQ, HCQ, RDV, GS441524, ARB, and GA, respectively (light blue, stick mode) with O6K-6Y2F complex. Red symbols, S1, S2, S3, and S4, indicate the canonical binding pockets for inhibitor's structural 'groups' alignment within the active site, and hydrogen bond interactions were represented with the green dotted line

offering insight into the impact of molecular architecture on inducing inhibitory activity. To the extent of our knowledge, the spatial orientation of these selected therapeutic inhibitors (as seen in Fig. 7) superimposed with reference standard O6K in a comparative manner is not yet reported in the literature. Further, all the docked structures are superposed to give overall comparative view (Fig. 8).

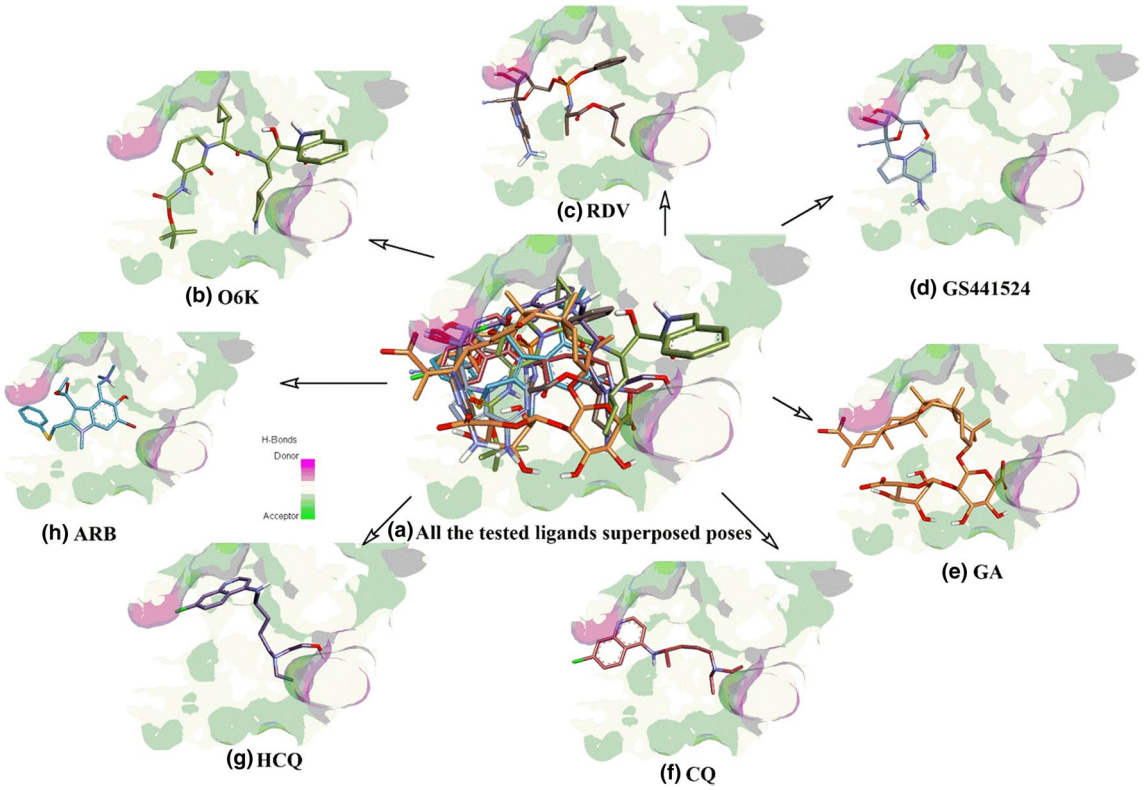


**Fig. 8** **a** Superposition poses of (i) O6K, (ii) RDV, (iii) GS441524, (iv) GA, (v) CQ, (vi) HCQ, and (vii) ARB corresponding binding to the same active pocket (binding domain) of SARS-CoV-2 $M^{pro}$ (PDB ID # 6Y2F). The SARS-CoV-2 Mpro catalytic domain is represented in surface mode

## Molecular dynamics (MD) simulations studies of GA and RDV with SARS-CoV-2 main protease (PDB ID # 6Y2F)

To confirm, validate, and explore the time-dependent interactions of ligands with the SARS-CoV-2 main protease (PDB ID # 6Y2F) and the stability of the ligand-receptor complex, a molecular dynamics study was performed. Based on the interactions with the binding pocket and binding energy calculation (Fig. 9, Table 1), we selected GA and RDV docked complexes to run MD simulation. The MD simulation was performed for 30 ns, and the dynamic stability of the complexes was analyzed using computational parameters like protein–ligand RMSD, L-RMSF, protein–ligand contacts, P-RMSF, ligand torsion profile, and ligand properties.

## Analysis of root mean square deviations of protein (RMSD-P), ligand root means square fluctuation (L-RMSF), and protein root mean square fluctuation (P-RMSF)

RMSD is the measure of the distance between the protein backbones of the superimposed protein. In order to determine the conformational stability of the protein backbone and ligand–protein complex, the RMSD analysis was monitored. RMSD-P is essentially studied to understand the movements of different atoms in the protein when the ligand

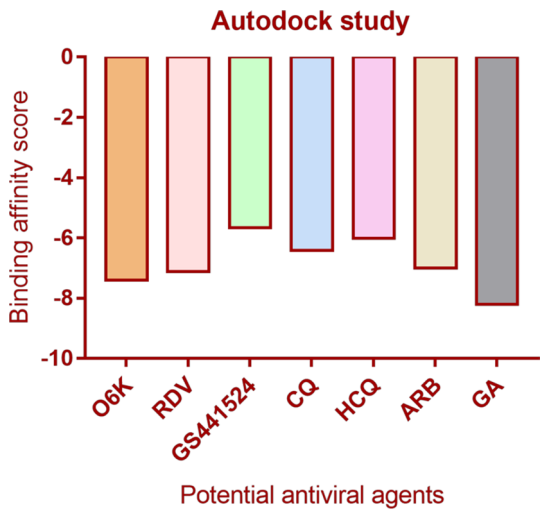


**Fig. 9** Binding free energy of tested drug molecules docked in the $M^{pro}$ pocket

is present in the active site of the receptor. This provides deep insight into the structural conformations of the protein throughout MD simulation. RMSD-P plot score was calculated for 30 ns. The RMSD-P plot for $M^{pro}$ complexes with **GA** was observed to be in the range of 1.0–2.25 Å (Fig. 10a), while for complexes with RDV, the value was in the range of 0.9 to 2.7 Å (Fig. 10b). Therefore, this result clearly indicates that the presence of **GA** and **RDV** in the active site of protein has maintained the stability of protein throughout the simulation period, but the stability was better in the presence of RDV. Furthermore, to determine the conformational stability of ligands with respect to protein, the RMSD-L was calculated. The RMSD-L for **GA** was found in the range of ~ 1.8–16 Å (Fig. 10a), while for RDV, it was found to be in the range of 2.4 to 5.4 Å (Fig. 10b). The graph of RMSD-P and RMSD-L specifies that the $M^{pro}$ ligand complex is stable over the period of the MD simulation. Among GA and RDV, RDV showed better interactions with the protein, which is the reason for the lesser RMSD values for RDV.

RMSF was calculated to predict the structural integrity of the protein backbone and $M^{pro}$ ligand complex. The RMSF graph of the $M^{pro}$ ligand complex (L-RMSF) and $M^{pro}$ (P-RMSF) is shown in Fig. 10c–f. The L-RMSF indicates that it is stable over the course of the simulation. **GA** atoms ranging from 9 to 20 are plotted to be highly fluctuated (RMSF > 3.0 Å, Fig. 10c), while for **RDV** atoms ranging from 10 to 18 (RMSF > 1.5 Å) and atoms ranging from 35–42 (RMSF > 1.0 Å, are highly fluctuated (Fig. 10d). Additionally, protein RMSF (P-RMSF) was calculated in order to measure the binding stability of the protein over the course of the MD simulation. In this plot, each peak indicates the protein area that fluctuates the most during the MD simulation (10e–f). Generally, tails (*N*- and *C*-terminal) fluctuate more than any other residues of the protein. For all the amino acid residues in the protein, the P-RMSF was below 4.0 Å when it was complexed with **GA** (Fig. 10e), and P-RMSF was below 3.6 Å when it was complexed with RDV (Fig. 10f).

The analysis of suitable protein–ligand interactions is an important aspect in order to identify the specific target site. In the docking studies, the H-bond was observed between hydroxy (OH) of the pyranose sugar and hydroxy (OH) of another pyranose sugar of **GA** with PHE140 and GLU166 residues (Fig. 11a). Furthermore, SER144 and GLN189 interact through hydrogen bonding with acid functionality (HO–C = O) of GA. In the MD simulation study, it was observed that one acid (COOH) group of compound **GA** formed polar interaction with GLY143, SER144, and HIS163. These interactions were observed to be stable over 34%, 55%, and 30%, respectively, of the simulation period. Furthermore, GLU166 is observed to form water-mediated interaction with the ligand for 34% of simulation time. Additionally, HIS172 showed polar interaction with the ligand for 31% of the simulation time. The bar diagram specifies the fraction of interactions with each amino acid residue over the course of the simulation run (Fig. 11c). In the case of RDV, the protein–ligand interactions indicate a cyclic ring formed π–π stacking interaction with HIS41, while the 3–OH group of sugar ring formed hydrogen with THR190 and GLN 192 and 4–OH group of sugar interacted with GLN-189, the nitrile group of the sugar ring formed a polar interaction with GLN192 (Fig. 11b). The complex also formed water-mediated interaction with ester functionality of RDV with HIS41, and the interaction was stable over 38% of the simulation run. The bifurcated water-mediated hydrogen bonding with ASN142 and GLU166 of the side chain amine nitrogen was observed.

In the case of RDV, it was observed that the complex forms hydrophobic and water bridge interaction with HIS41 for 81% and 90% of the simulation period while forming water bridge interaction with ASN142, and GLU166 for 46% and 36% during the entire simulation run (Fig. 11b). The complex also formed hydrogen bonds with GLN189, THR190, and GLN192 for 91%, 83%, 48%, and 56% of the entire simulation run (Fig. 11b). The bar diagram specifies the fraction of interactions of **RDV** with each amino acid residue over the course of the simulation run (Fig. 11d).

## *In silico* physicochemical and ADMET properties of CQ, HCQ, ABD, RDV, GS441524, and GA using admetSAR software

The calculation of physicochemical parameters and ADMET prediction was carried out on online available *admetSAR* software [52]. The compounds CQ, HCQ, and ARB were predicted to be positive toward Ames mutagenesis, whereas GA, RDV, and its active metabolite (GS441524) showed negative results for Ames mutagenesis. CQ is underlying in toxic category II (moderately toxic and moderately irritating), while HCQ, ARB, RDV, and GS441524 are in toxic category III (slightly toxic and slightly irritating) in terms of acute oral toxicity. The GA falls in the IV category (non-toxic) in terms of acute oral toxicity. The compounds CQ, HCQ, ARB, and RDV were predicted to show substantial aromatase binding and blood–brain barrier (BBB) permeability properties. The ability of CQ and HCQ for transverse BBB is less known [53], which is not in favor of predicted BBB permeability property. Both ARB and RDV were predicted to show androgen receptor binding, while CQ and HCQ do not show such type of binding. The entire compounds showed inhibition of OATP1B1, OATP1B3, and BSEP transporter. The compounds CQ, HCQ, and ARB were predicted as inhibitors of OCT1 transporter, whereas RDV does not inhibit OCT1 transporter. None of the four compounds CQ, HCQ, ABD, and RDV were predicted to show the inhibition of BRCP, OATP2B1, and OCT2

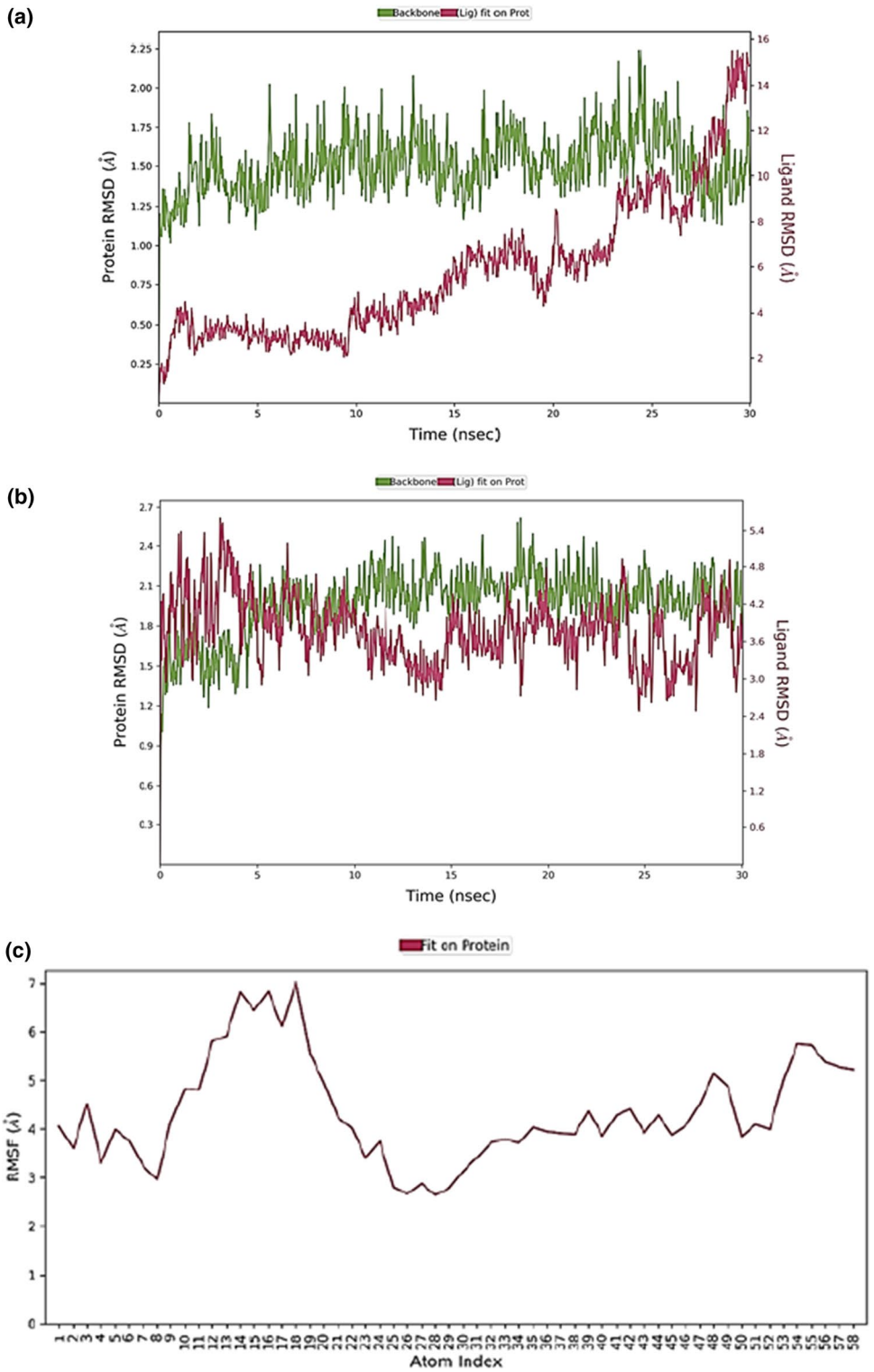


**Fig. 10** **a**, **b** Plot of protein and ligand RMSD values as a function of time. Protein RMSD at the left Y-axis and the ligand RMSD at the right Y-axis coordinates, whereas ligands are **GA** and **RDV,** respectively, with SARS-CoV-2 $M^{pro}$ (PDB ID # 6Y2F). **c**, **d** L-RMSF **GA** and **RDV,** respectively. **e, f** P-RMSF of **GA** and **RDV,** respectively

**Fig. 10** (continued)

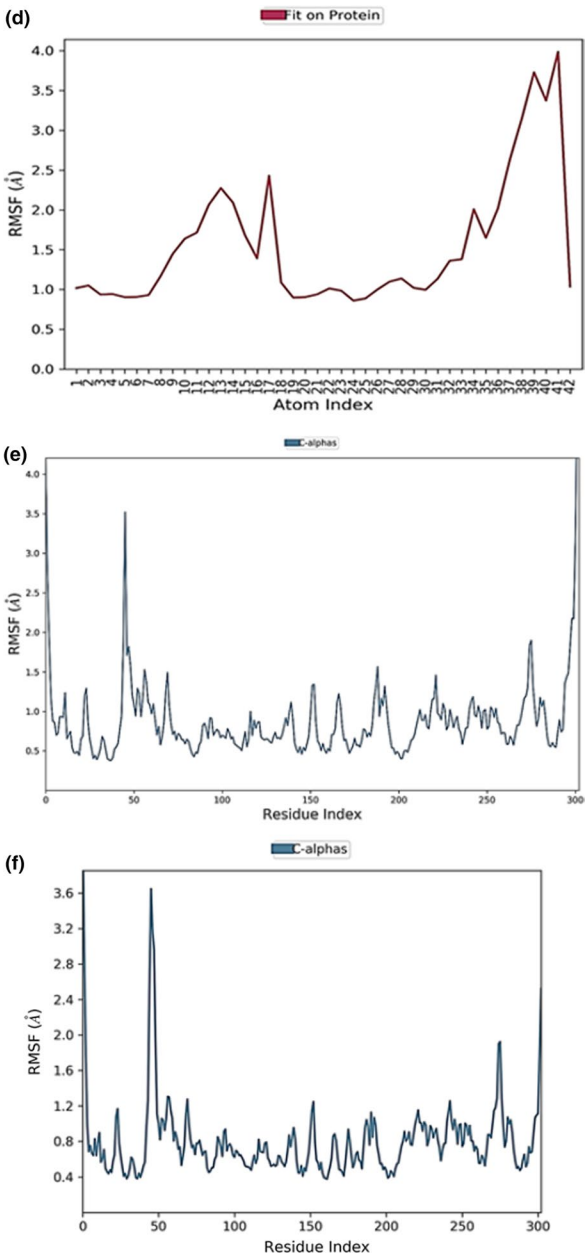


transporter. The compound CQ and HCQ were predicted as a substrate of CYP3A4, which are following the reported property [54]. The non-inhibitory activity of CQ and HCQ against CYP3A4 based on an *in vitro* assay, which is also found following the predicted CYP properties, has been documented in recent research work by Li et al., 2020 [55]. The compounds ABD, GA, GS441524, and RDV were also predicted as a substrate of CYP3A4 but did not turn out to be the inhibitor of CYP3A4. The compounds ARB, RDV, GS441524, and GA were neither the substrate of CYP2C9 nor the inhibitor of CYP2C9. Both CQ and HCQ were predicted as the substrate of CYP2D6, which is true as per the published literature [54], while ABD and RDV are not. All compounds are predicted to not act as an inhibitor of CYP2D6, which is in contrast to the reported literature [56]. All the compounds CQ, HCQ, and RDV were predicted as non-inhibitor of CYP1A2, CYP2C9, and CYP inhibitory

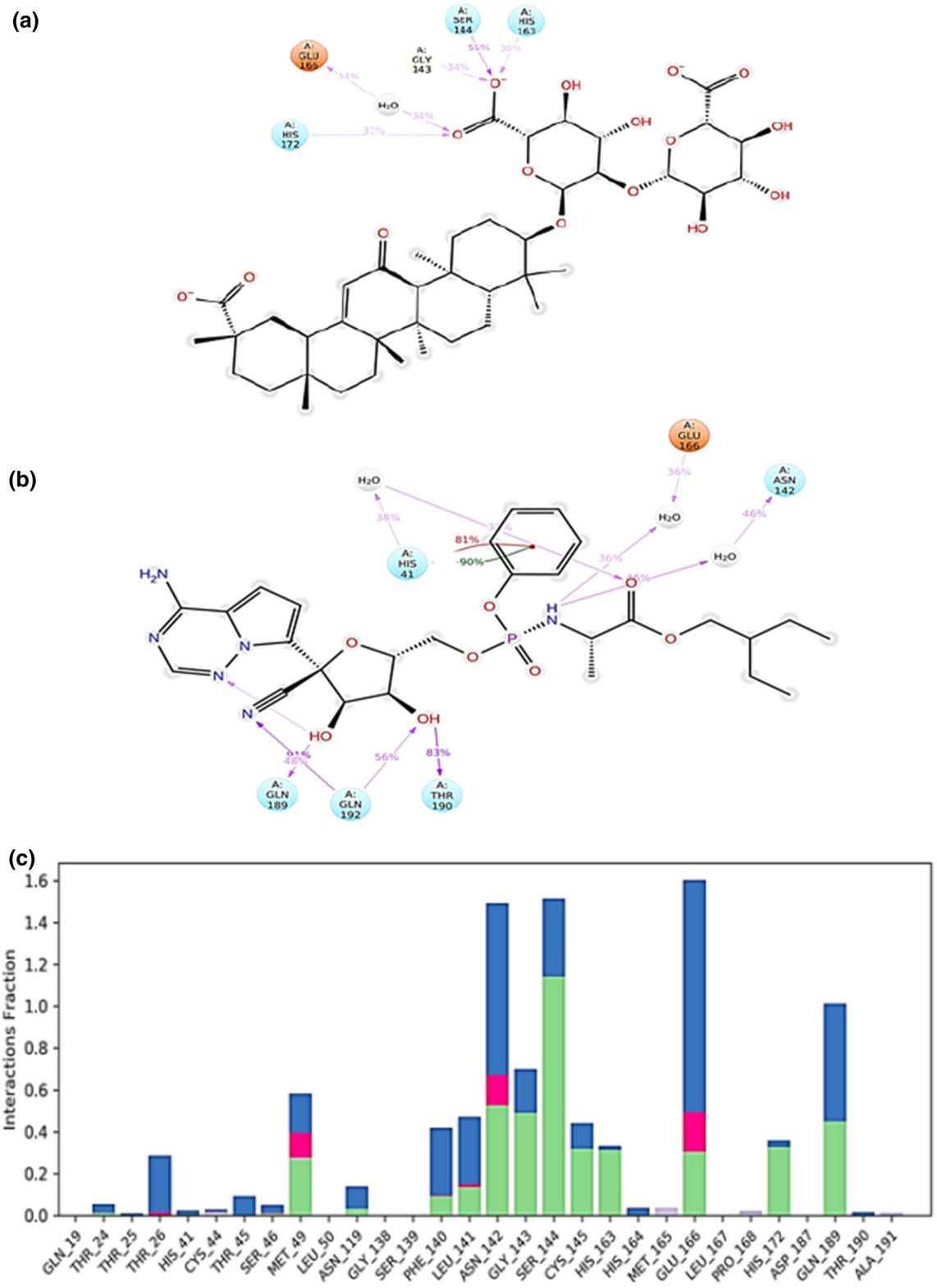


**Fig. 11** **a**, **b** A schematic of detailed **GA** and **RDV** atoms interactions with the key amino acid residues. **c**, **d** Bar charts of protein interaction with ligands **GA** and **RDV** as monitored throughout the simulation (green—H-bonding; gray—hydrophobic; blue—water bridges; pink—ionic interactions)

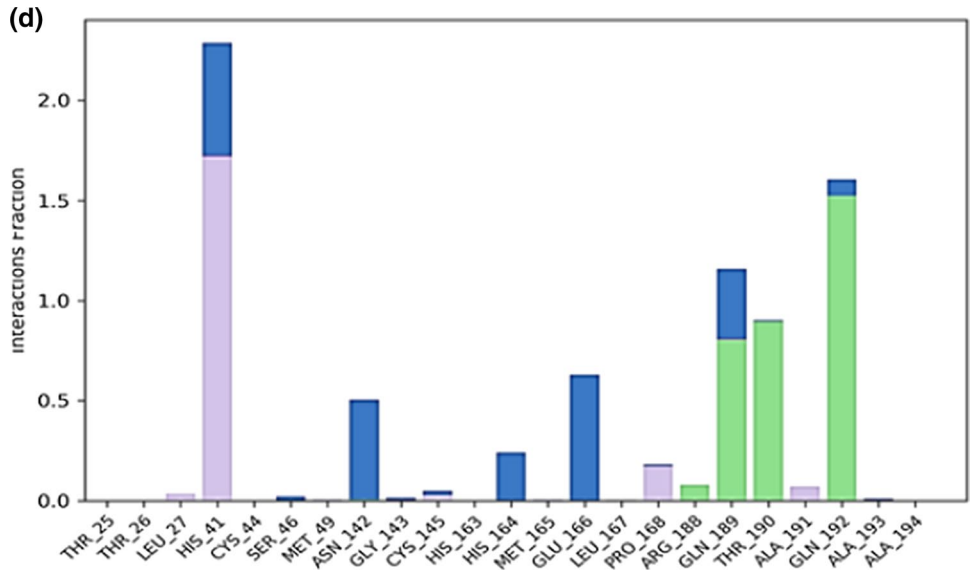


**Fig. 11** (continued)

promiscuity except ABD. It is well reported in the literature that CQ and HCQ are metabolized by several of the CYP450 subfamilies (2C8, 3A4/5, 2D6), mainly to their desethylation form (desethylchloroquine or desethylhydroxychloroquine) and the derived metabolites are biologically active [57]. ABD experiences major metabolic activity by CYP3A4, whereas to a lesser extent by other P450s and flavin-containing monooxygenases (FMOs) [58], and it is well documented that ARB has strong inducers/inhibitors of CYP3A4, which is in close relation with the predicted CYP activity [54].

The *in vitro* study implicated that RDV is a substrate for CYP2C8, CYP2D6, and CYP3A4, P-gp, OATP1B1, and esterases [59], which is found true for the predicted CYP3A4 and P-gp property. In vitro inhibitory activity against CYP3A4, OATP1B1 and OATP1B3 has been reported for RDV [60, 61], which is conversely to the predicted properties for CYP3A4 and OATP1B1. The compounds CQ, HCQ, ABD were predicted to show a positive response to Caco-2 (intestinal permeability test) except RDV. None of the compounds were predicted to show binary carcinogenicity, eye irritation, and eye corrosion property. Compound CQ and HCQ were predicted to show estrogen receptor binding and glucocorticoid receptor binding affinities, while ABD and RDV did not show binding affinity to these receptors. Except HCQ, all the compounds were predicted to demonstrated hepatotoxicity.

An explicitly marked difference in hERG activity of CQ and HCQ enantiomers was found in a study by Li et al., suggesting that the optimal protection profile could be obtained from pure S-HCQ (hERG $IC_{50} > 20$ μM), and no prolongation of QT was found with S-HCQ alone [62]. Oral bioavailability has only been seen by CQ and HCQ, but all the compounds show human intestinal absorption. None of the compounds were predicted as MATE inhibitors. HCQ is predicted to show higher acute oral toxicity, followed by CQ, ABD, and RDV. The compound RDV is predicted to have higher plasma protein binding followed by ARB, HCQ, and CQ, respectively, which is found in accordance with the reported values for RDV (88–93.6%), CQ (46–74%) [63], and HCQ (64%) [64], except for the ARB. UGT prediction suggested that only HCQ and ABD act as UGT substrates, while CQ and RDV do not. All the compounds were predicted to possess thyroid receptor binding (Table 2).

The solubility and lipophilicity play an important role in assessing the potential of molecules as a therapeutic agent. All the molecules in this study were found to behave in a similar manner in terms of their predicted solubility (Table 3) except HCQ and GS441524. The lipophilicity parameter of the molecules was found to be in the range of -1.092 to 5.11, as shown in Table 3. A study by Warhurst et al. 2003 reported experimental log P of HCQ ($3.84 \pm 0.2$) and CQ (4.72), which were in good agreement with their calculated ClogP values and ~$0.30 \pm 0.04$ log units lower than the calculated ClogP value [65]. The log P of the RDV and GS441524 is 1.8 and 1.65, respectively, which are in good agreement with their calculated ClogP values, but a significant variation was observed in the case of GS441524 with − 3.84 log units higher than the calculated ClogP [66]. On the contrary, GA undergoes presystemic biotransformation after oral administration to glycyrrhetinic acid (GLA); therefore, most of the clinical pharmacokinetic studies are published on GLA.

**Table 2** The ADMET properties for CQ, HCQ, ARB, RDV, GS441524, and GA using online *admetSAR* prediction software (version 2.0)

| Property | CQ | HCQ | ARB | RDV | GS441524 | GA |
|---|---|---|---|---|---|---|
| Ames toxicity | + | + | + | − | − | − |
| Acute oral toxicity (c) | II | III | III | III | III | IV |
| Blood–brain barrier | + | + | + | − | + | − |
| Caco−2 permeability | + | − | + | − | − | − |
| CYP1A2 inhibition | − | − | + | − | − | − |
| CYP2C9 substrate | + | + | − | − | − | − |
| CYP2D6 inhibition | − | − | − | − | − | − |
| CYP2D6 substrate | + | + | − | − | − | − |
| CYP3A4 inhibition | − | − | − | − | − | − |
| CYP3A4 substrate | + | + | + | + | − | + |
| CYP inhibitory promiscuity | Low | Low | Low | Low | Low | Low |
| HERG inhibition | Weak | Weak | Weak | Weak | Weak | Weak |
| Intestinal absorption | + | + | + | + | + | + |
| cLogP[#] | 5.06 | 4.11 | 5.49 | 1.24 | −2.19 | 3.03 |
| Molecular weight | 319.88 | 335.88 | 477.72 | 602.58 | 291.27 | 822.94 |
| ROCT | Inhibitor | Non-inhibitor | Inhibitor | Non-inhibitor | Non-inhibitor | Non-inhibitor |
| PGP-inhibitor | Inhibitor | −/+ | −/+ | − | − | −/+ |
| PGP-substrate | + | + | + | + | − | + |
| S.L | Lysosome | Lysosome | Lysosome | Lysosome | Lysosome | Mitochondria |
| Water solubility | −4.348 | −3.565 | −4.367 | −3.473 | −2.167 | −4.512 |

*HERG* human either-a-go-go inhibition, *HBD* hydrogen bond donor, *HBA* hydrogen bond acceptor, *PGP* P-glycoprotein inhibitor, *PPB* plasma protein binding, *SL* subcellular localization; *ROCT* renal organic cation transporter

Interestingly, the presence of sugar moiety attached to GA brings its lipophilicity to the desired range as per ' 'Lipinski's rule [67]. The permeability and distribution properties ($V_d$) are directly related to lipophilicity. Therefore, a similar trend was observed in terms of effective permeability and distribution properties ($V_d$) except compound GS441524. The compounds CQ, HCQ, ARB were predicted to be P-gp substrate while RDV, GS441524, and GA were not found to be P-gp substrates. The compounds CQ and HCQ were predicted as the substrate of P-glycoprotein but not the inhibitor of P-glycoprotein, while it is reported that CQ and HCQ can potentially inhibit P-glycoprotein efflux pumps [57], whereas ABD and RDV predicted as an inhibitor P-glycoprotein but not the substrate of P-glycoprotein. All the molecules in this study except ARB were predicted as not the inhibitors of the OATP1B1. CQ and HCQ were predicted as an inhibitor of organic cations transporter 2 (OCT2) but turn out to be devoid of inhibitors of bile salt export pump (BSEP), whereas ARB and RDV showed the reverse trends as observed with CQ and HCQ. Intriguingly, GS441524 and GA were turn out to be neither the inhibitor of OCT2 nor the inhibitor of BSEP transporter. Interestingly, RDV was predicted as the breast cancer resistance protein (BCRP) substrate among the molecules in this study. The metabolism through cytochrome (CYP) plays an important role in drug disposition. HCQ and GA were predicted as the substrate for CYP2B6, while CQ, HCQ, and GA were also found to be the substrate for CYP2C8.

Additionally, CQ, ARB, and GA can also be utilized by CYP2C19, and CYP3A4 was predicted to utilize CQ, ARB, RDV, and GA as a substrate. The inhibition potential of all six compounds was also expected along with substrate prediction. CQ was predicted to be an inhibitor of CYP1A2, while ARB and RDV were assessed to be an inhibitor of CYP3A4, while all other compounds were not found to be an inhibitor of CYP. Prediction of uridine glucuronosyltransferase (UGT) substrate suggested that ARB to be a substrate of UGT1A1, while CQ, HQ, ARB, and GS441524 were assessed to be a substrate of UGT2B7. In terms of skin sensitivity, CQ and HCQ were predicted to be skin sensitive, while ARB and GA were assessed to be respiratory sensitive. CQ, HCQ, and GA were predicted to induce phospholipidosis. CQ and HCQ are known to be non-selective inhibitors of various phospholipase A2 ($PLA_2$) isoforms and are thought to act by altering the pH of lysosomes [53], which is shown to be closely similar to the predicted property. In terms of reproductive toxicity, ARB and RDV were predicted as toxic and these molecules were found to be mild to moderate hepatotoxic as indicated by elevated levels of marker enzymes of hepatotoxicity. The predicted hepatotoxicity of the RDV is found true with the experimental indication, as evidence for its hepatotoxic effects in

**Table 3** The ADMET prediction for CQ, HCQ, ARB, RDV, GS441524, and GA using ADMET Predictor™

| ADMET properties | Identifier | CQ | HCQ | ARB | RDV | GS441524 | GA |
|---|---|---|---|---|---|---|---|
| Ionization | S + Acidic.pKa | None | 9.66 | None | 10.93 | None | None |
| Solubility | S + Sw | 0.099 | 0.558 | 0.11 | 0.023 | 2.601 | 2.965 |
| Lipophilicity | S + logP | 5.113 | 3.937 | 4.692 | 1.597 | -1.092 | 2.402 |
| Permeability | S + Peff ($cm/s \times 10^{-4}$) | 1.287 | 0.948 | 3.208 | 0.084 | 0.297 | 3.707 |
| Pharmacokinetic | $V_d$ (l/kg) | 10.63 | 7.071 | 0.859 | 1.19 | 1.253 | 2.433 |
| Transporter | Pgp substrate | Yes (83%) | Yes (94%) | Yes (94%) | No (93%) | No (93%) | No (81%) |
| | OATP1B1_Inh | No (98%) | No (98%) | Yes (42%) | No (98%) | No (98%) | No (98%) |
| | OCT2_Inh | Yes (92%) | Yes (92%) | No (78%) | No (84%) | No (85%) | No (95%) |
| | BSEP_Inh | No (99%) | No (99%) | Yes (38%) | Yes (36%) | No (99%) | No (92%) |
| | BCRP substrate | No (65%) | No (67%) | No. (95%) | Yes (79%) | No (67%) | No (95%) |
| CYP substrates | CYP2B6 | No (98%) | Yes (64%) | No (97%) | No (97%) | No (84%) | Yes (79%) |
| | CYP2C8 | Yes (63%) | Yes (45%) | No (97%) | No (97%) | No (98%) | Yes (64%) |
| | CYP2C19 | Yes (36%) | No (82%) | Yes (38%) | No (98%) | No (98%) | Yes (71%) |
| | CYP3A4 | Yes (77%) | No (37%) | Yes (98%) | Yes (79%) | No (84%) | Yes (88%) |
| Enzyme kinetics | CYP3A4_*Km* | 161.101 | Non-substrate | 14.087 | 8.770 | Non-substrate | 591.623 |
| | CYP3A4_$V_{max}$ | 8.880 | Non-substrate | 3.644 | 33.522 | Non-substrate | 65.951 |
| | CYP3A4_CLint | 6.119 | Non-substrate | 28.714 | 424.275 | Non-substrate | 12.374 |
| CYP inhibition | CYP1A2 | Yes (53%) | No (79%) | No (90%) | No (64%) | No (97%) | No (97%) |
| | CYP2C19 | No (93%) | No (99%) | No (99%) | No (99%) | No (99%) | No (97%) |
| | CYP3A4 | No (74%) | No (66%) | Yes (80%) | Yes (80%) | No (69%) | No (94%) |
| Inhibition kinetics | CYP3A4_Inh. midaz | No (79%) | No (79%) | Yes (75%) | No (55%) | No (68%) | Yes (63%) |
| | CYP3A4_Ki. midaz | 80.941 | 119.823 | 26.841 | 0.594 | 4.112 | 36.199 |
| UGT substrates | UGT1A1 | No (97%) | No (97%) | Yes (77%) | No (66%) | No (89%) | No (99%) |
| | UGT1A10 | No (97%) | No (97%) | No (97%) | No (75%) | No | No (97%) |
| | UGT2B7 | Yes (93%) | Yes (93%) | Yes (70%) | No (52%) | Yes (85%) | No (96%) |
| Skin sensitivity | Sens_skin | Sensitive (95%) | Sensitive (61%) | Non-sensitive (52%) | Non-sensitive | Non-sensitive | Non-sensitive (85%) |
| Respiratory sensitivity | Sens.resp | Non-sensitive (60%) | Non-sensitive (98%) | Sensitive (56%) | Non-sensitive (73%) | Non-sensitive (57%) | Sensitive (77%) |
| Chromosomal Aberr | Chrom.Aberr | Non-toxic (56%) | Non-toxic (59%) | Non-toxic (69%) | Non-toxic (63%) | Non-toxic (68%) | Non-toxic (88%) |
| Phospholipidosis | PLipidosis | Toxic (95%) | Toxic (95%) | Non-toxic (63%) | Non-toxic (99%) | Non-toxic (99%) | Toxic (74%) |
| Reproductive toxicity | Repro.Tox | Non-toxic (97%) | Non-toxic (97%) | Toxic (53%) | Toxic (62%) | Non-toxic (67%) | Non-toxic (97%) |
| Hepatotoxicity | Ser_Alkphos | Normal (92%) | Normal (96%) | Elevated (50%) | Elevated (90%) | Elevated (96%) | Normal (92%) |
| | Ser.GGT | Normal (97%) | Normal (97%) | Normal (97%) | Normal (87%) | Elevated (72%) | Elevated (65%) |
| | Ser.LDH | Normal (77%) | Normal (77%) | Elevated (59%) | Normal (87%) | Elevated (50%) | Normal (87%) |
| | Ser.AST | Normal (91%) | Normal (91%) | Normal (78%) | Normal | Elevated (89%) | Elevated (46%) |
| | Ser.ALT | Normal (94%) | Normal (94%) | Normal (94%) | Elevated (66%) | Elevated (94%) | Normal (67%) |
| Risks | Absn.Risk | 0 | 1.227 | 1.227 | 6 | 2.666 | 0 |
| | CYP.Risk | 0.121 | 0.55 | 0.55 | 3 | 0 | 1 |
| | MUT.Risk | 2.1 | 0.6 | 0.6 | 0 | 1.2 | 0 |
| | TOX.Risk | 1.977 | 0 | 0 | 1 | 4 | 1 |
| | ADMET.Risk | 3.078 | 1.846 | 1.846 | 10 | 6.666 | 2 |

transplanted patients is already being documented in the literature [62]. GA has been reported to have the potential to reduce hepatocyte inflammation to some extent, which is in close proximity to the predicted properties [62].

## Conclusion

Here, we report the docking studies of the clinically oriented molecules, which have shown promising anti-COVID-19 activity. In view of the current pandemic situation and the dearth of therapeutic agents against SARS-CoV-2, the present docking study revealed the potential application of the selected therapeutic agents possesses moderate to excellent binding in the O6K binding pocket with variable binding affinity from -5.66 to -8.21 kcal/ mol. The present finding highlights silent features of the active domain [binding pocket(s)] accessible for ligand interaction within the target macromolecule and reveals the spatial orientation of best conformers, which may aid in designing novel inhibitors for SARS-CoV-2 main protease. The docking studies of the selected therapeutics showed that within the active substrate-binding pocket of $M^{pro}$, CYS145, HIS163, and GLU166 are the specific amino acid residues involved interaction with target molecules. This signifies their importance as key residues that can facilitate the substrate–ligand complex formation and modulate the function of $M^{pro}$ as potential inhibitors. At the active site of $M^{pro}$, the spatial orientations of clinically oriented molecules may give an insight into the possible structural changes to be made to further strengthen the binding affinity at the active site. The lower RMSD values from the MD studies for RDV imply that RDV has better interactions with the protein. The molecules' ADMET prediction might help in the successful repurposing of these molecules against the new target. The present study could serve as a guide to analyze the crucial role of active site residues and their impact on enzyme inhibitory activity. We believe that this study might help researchers develop future therapeutic agents of high selectivity and efficacy to achieve effective treatment of COVID-19. However, additional exploration in terms of *in vivo* efficacy is inevitable for assessing these drugs' clinical applicability in a more effective manner.

**Acknowledgements** GM is thankful to the Indian Institute of Technology (BHU). GM is thankful to Simulation Plus, Lancaster, CA, USA, to provide a trial version of ADMET Prediction™ (version 9.5). AB, LJ, and YSP are thankful to the Indian Institute of Technology (BHU) and MHRD, India, for fellowship. Project grant support through SERB funding [CVD/2020/000031] to VKD and GPM is acknowledged.

## Compliance with ethical standards

**Conflict of interest** The authors declare that there is no conflict of interest in this work.

## References

1. Guo Y-R, Cao Q-D, Hong Z-S, Tan Y-Y, Chen S-D, Jin H-J, Tan K-S, Wang D-Y, Yan Y (2020) The origin, transmission and clinical therapies on coronavirus disease 2019 (COVID-19) outbreak—an update on the status. Mil Med Res 7(1):11–11. https://doi.org/10.1186/s40779-020-00240-0
2. WHO (2020) https://www.who.int/docs/default-source/coronaviruse/situation-reports/20200408-sitrep-79-covid-19.pdf?sfvrsn=4796b143_4
3. Zhai P, Ding Y, Wu X, Long J, Zhong Y, Li Y (2020) The epidemiology, diagnosis and treatment of COVID-19. Int J Antimicrob Agents:105955. https://doi.org/10.1016/j.ijantimicag.2020.105955
4. Lai C-C, Shih T-P, Ko W-C, Tang H-J, Hsueh P-R (2020) Severe acute respiratory syndrome coronavirus 2 (SARS-CoV-2) and coronavirus disease-2019 (COVID-19): the epidemic and the challenges. Int J Antimicrob Agents 55(3):105924–105924. https://doi.org/10.1016/j.ijantimicag.2020.105924
5. Zhang L, Lin D, Kusov Y, Nian Y, Ma Q, Wang J, von Brunn A, Leyssen P, Lanko K, Neyts J, de Wilde A, Snijder EJ, Liu H, Hilgenfeld R (2020) α-Ketoamides as broad-spectrum inhibitors of coronavirus and enterovirus replication: structure-based design, synthesis, and activity assessment. J Med Chem 63(9):4562–4578. https://doi.org/10.1021/acs.jmedchem.9b01828
6. Liu C, Zhou Q, Li Y, Garner LV, Watkins SP, Carter LJ, Smoot J, Gregg AC, Daniels AD, Jervey S, Albaiu D (2020) Research and development on therapeutic agents and vaccines for COVID-19 and related human coronavirus diseases. ACS Cent Sci 6(3):315–331. https://doi.org/10.1021/acscentsci.0c00272
7. Zhu Y, Li J, Pang Z (2020) Recent insights for the emerging COVID-19: Drug discovery, therapeutic options and vaccine development. Asian J Pharm Sci. https://doi.org/10.1016/j.ajps.2020.06.001
8. Hotez PJ, Corry DB, Bottazzi ME (2020) COVID-19 vaccine design: the Janus face of immune enhancement. Nat Rev Immunol 20(6):347–348. https://doi.org/10.1038/s41577-020-0323-4
9. Wilder-Smith A, Chiew CJ, Lee VJ (2020) Can we contain the COVID-19 outbreak with the same measures as for SARS? Lancet Infect Dis. https://doi.org/10.1016/S1473-3099(20)30129-8
10. Lu R, Zhao X, Li J, Niu P, Yang B, Wu H, Wang W, Song H, Huang B, Zhu N, Bi Y, Ma X, Zhan F, Wang L, Hu T, Zhou H, Hu Z, Zhou W, Zhao L, Chen J, Meng Y, Wang J, Lin Y, Yuan J, Xie Z, Ma J, Liu WJ, Wang D, Xu W, Holmes EC, Gao GF, Wu G, Chen W, Shi W, Tan W (2020) Genomic characterisation and epidemiology of 2019 novel coronavirus: implications for virus origins and receptor binding. Lancet 395(10224):565–574. https://doi.org/10.1016/S0140-6736(20)30251-8
11. Beigel JH, Tomashek KM, Dodd LE, Mehta AK, Zingman BS, Kalil AC, Hohmann E, Chu HY, Luetkemeyer A, Kline S, Lopez de Castilla D, Finberg RW, Dierberg K, Tapson V, Hsieh L, Patterson TF, Paredes R, Sweeney DA, Short WR, Touloumi G, Lye DC, Ohmagari N, Oh M-d, Ruiz-Palacios GM, Benfield T, Fätkenheuer G, Kortepeter MG, Atmar RL, Creech CB, Lundgren J, Babiker AG, Pett S, Neaton JD, Burgess TH, Bonnett T, Green M, Makowski M, Osinusi A, Nayak S, Lane HC (2020) Remdesivir for the treatment of Covid-19 —Preliminary Report. Doi: https://doi.org/10.1056/NEJMoa2007764

12. Rosa SGV, Santos WC (2020) Clinical trials on drug repositioning for COVID-19 treatment. Revista panamericana de salud publica = Pan Am J Public Health 44:e40–e40. https://doi.org/10.26633/RPSP.2020.40
13. Chen YW, Yiu C-PB, Wong K-Y (2020) Prediction of the SARS-CoV-2 (2019-nCoV) 3C-like protease (3CL (pro)) structure: virtual screening reveals velpatasvir, ledipasvir, and other drug repurposing candidates. F1000Research. https://doi.org/10.12688/f1000research.22457.1
14. Senanayake SL (2020) Drug repurposing strategies for COVID-19. Futur Drug Discov. https://doi.org/10.4155/fdd-2020-0010
15. Fantini J, Scala CD, Chahinian H, Yahi N (2020) Structural and molecular modeling studies reveal a new mechanism of action of chloroquine and hydroxychloroquine against SARS-CoV-2 infection. Int J Antimicrob Agents. https://doi.org/10.1016/j.ijantimicag.2020.105960
16. Fan HH, Wang LQ, Liu WL, An XP, Liu ZD, He XQ, Tong YG (2020) Repurposing of clinically approved drugs for treatment of coronavirus disease 2019 in a 2019-novel coronavirus-related coronavirus model. Chin Med J. https://doi.org/10.1097/cm9.0000000000000797
17. Cao B, Wang Y, Wen D, Liu W, Wang J, Fan G, Ruan L, Song B, Cai Y, Wei M, Li X, Xia J, Chen N, Xiang J, Yu T, Bai T, Xie X, Zhang L, Li C, Yuan Y, Chen H, Li H, Huang H, Tu S, Gong F, Liu Y, Wei Y, Dong C, Zhou F, Gu X, Xu J, Liu Z, Zhang Y, Li H, Shang L, Wang K, Li K, Zhou X, Dong X, Qu Z, Lu S, Hu X, Ruan S, Luo S, Wu J, Peng L, Cheng F, Pan L, Zou J, Jia C, Wang J, Liu X, Wang S, Wu X, Ge Q, He J, Zhan H, Qiu F, Guo L, Huang C, Jaki T, Hayden FG, Horby PW, Zhang D, Wang C (2020) A trial of Lopinavir-Ritonavir in adults hospitalized with severe Covid-19. New Engl J Med 382:1787–1799
18. Sweiti H, Ekwunife O, Jaschinski T, Lhachimi SK (2017) Repurposed therapeutic agents targeting the ebola virus: a systematic review. Curr Therapeutic Res 84:10–21. https://doi.org/10.1016/j.curtheres.2017.01.007
19. Zhao Z, Martin C, Fan R, Bourne PE, Xie L (2016) Drug repurposing to target Ebola virus replication and virulence using structural systems pharmacology. BMC Bioinf 17:90–90. https://doi.org/10.1186/s12859-016-0941-9
20. Cheng F, Murray JL, Rubin DH (2016) Drug repurposing: new treatments for Zika virus infection? Trends Mol Med 22(11):919–921. https://doi.org/10.1016/j.molmed.2016.09.006
21. Baker JD, Uhrich RL, Kraemer GC, Love JE, Kraemer BC (2020) A drug repurposing screen identifies hepatitis C antivirals as inhibitors of the SARS-CoV-2 main protease. bioRxiv:2020.2007.2010.197889. doi: https://doi.org/10.1101/2020.07.10.197889
22. Devaux CA, Rolain J-M, Colson P, Raoult D (2020) New insights on the antiviral effects of chloroquine against coronavirus: what to expect for COVID-19? Int J Antimicrobl Agents. https://doi.org/10.1016/j.ijantimicag.2020.105938
23. Touret F, de Lamballerie X (2020) Of chloroquine and COVID-19. Antiviral Res 177:104762. https://doi.org/10.1016/j.antiviral.2020.104762
24. Wang X, Cao R, Zhang H, Liu J, Xu M, Hu H, Li Y, Zhao L, Li W, Sun X, Yang X, Shi Z, Deng F, Hu Z, Zhong W, Wang M (2020) The anti-influenza virus drug, arbidol is an efficient inhibitor of SARS-CoV-2 in vitro. Cell Discov 6(1):28. https://doi.org/10.1038/s41421-020-0169-8
25. Al-Bari MAA (2017) Targeting endosomal acidification by chloroquine analogs as a promising strategy for the treatment of emerging viral diseases. Pharmacol Res Perspect 5(1):e00293–e00293. https://doi.org/10.1002/prp2.293
26. Al-Tawfiq JA, Al-Homoud AH, Memish ZA (2020) Remdesivir as a possible therapeutic option for the COVID-19. Travel Med Infect Dis. https://doi.org/10.1016/j.tmaid.2020.101615
27. Morse JS, Lalonde T, Xu S, Liu WR (2020) Learning from the past: possible urgent prevention and treatment options for severe acute respiratory infections caused by 2019-nCoV. ChemBioChem 21(5):730–738. https://doi.org/10.1002/cbic.202000047
28. Sheahan TP, Sims AC, Leist SR, Schäfer A, Won J, Brown AJ, Montgomery SA, Hogg A, Babusis D, Clarke MO, Spahn JE, Bauer L, Sellers S, Porter D, Feng JY, Cihlar T, Jordan R, Denison MR, Baric RS (2020) Comparative therapeutic efficacy of remdesivir and combination lopinavir, ritonavir, and interferon beta against MERS-CoV. Nat Commun 11(1):222. https://doi.org/10.1038/s41467-019-13940-6
29. Boriskin YS, Leneva IA, Pecheur EI, Polyak SJ (2008) Arbidol: a broad-spectrum antiviral compound that blocks viral fusion. Curr Med Chem 15(10):997–1005. https://doi.org/10.2174/092986708784049658
30. He J, Hu L, Huang X, Wang C, Zhang Z, Wang Y, Zhang D, Ye W (2020) Potential of coronavirus 3C-like protease inhibitors for the development of new anti-SARS-CoV-2 drugs: Insights from structures of protease and inhibitors. Int J Antimicrob Agents 56(2):106055. https://doi.org/10.1016/j.ijantimicag.2020.106055
31. Luo P, Liu D, Li J (2020) Pharmacological perspective: glycyrrhizin may be an efficacious therapeutic agent for COVID-19. Int J Antimicrob Agents 55(6):105995. https://doi.org/10.1016/j.ijantimicag.2020.105995
32. Zhang L, Lin D, Sun X, Curth U, Drosten C, Sauerhering L, Becker S, Rox K, Hilgenfeld R (2020) Crystal structure of SARS-CoV-2 main protease provides a basis for design of improved α-ketoamide inhibitors. Science 368(6489):409–412. https://doi.org/10.1126/science.abb3405
33. Huynh T, Wang H, Luan B (2020) In Silico Exploration of the Molecular Mechanism of Clinically Oriented Drugs for Possibly Inhibiting SARS-CoV-' '2's Main Protease. J Phys Chem Lett 11(11):4413–4420. https://doi.org/10.1021/acs.jpclett.0c00994
34. Savelieff MG, Lee S, Liu Y, Lim MH (2013) Untangling amyloid-β, tau, and metals in Alzheimer's disease. ACS Chem Biol 8(5):856–865. https://doi.org/10.1021/cb400080f
35. Berman HM, Westbrook J, Feng Z, Gilliland G, Bhat TN, Weissig H, Shindyalov IN, Bourne PE (2000) The protein data bank. Nucleic Acids Res 28(1):235–242. https://doi.org/10.1093/nar/28.1.235
36. Hanwell MD, Curtis DE, Lonie DC, Vandermeersch T, Zurek E, Hutchison GR (2012) Avogadro: an advanced semantic chemical editor, visualization, and analysis platform. J Cheminform 4(1):17–17. https://doi.org/10.1186/1758-2946-4-17
37. Sarukhanyan E, Shityakov S, Dandekar T (2020) Rational drug design of Axl tyrosine kinase type I inhibitors as promising candidates against cancer. Front Chem 7:920. https://doi.org/10.3389/fchem.2019.00920
38. Research DES (2019) Desmond molecular dynamics system, in maestro-desmond interoperability tools (Research, D. E. S., Ed.), Schrödinger, . New York
39. Simulations Plus I (2020) ADMET predictor (2020) Simulations plus, Inc., Lancaster, CA. Simulations plus, Inc., Lancaster, CA
40. Jin Z, Du X, Xu Y, Deng Y, Liu M, Zhao Y, Zhang B, Li X, Zhang L, Peng C, Duan Y, Yu J, Wang L, Yang K, Liu F, Jiang R, Yang X, You T, Liu X, Yang X, Bai F, Liu H, Liu X, Guddat LW, Xu W, Xiao G, Qin C, Shi Z, Jiang H, Rao Z, Yang H (2020) Structure of Mpro from SARS-CoV-2 and discovery of its inhibitors. Nature 582(7811):289–293. https://doi.org/10.1038/s41586-020-2223-y
41. Kumar Y, Singh H, Patel CN (2020) In silico prediction of potential inhibitors for the main protease of SARS-CoV-2 using molecular docking and dynamics simulation based drug-repurposing.

J Inf Publ Health 13(9):1210–1223. https://doi.org/10.1016/j.jiph.2020.06.016
42. Wang J (2020) Fast Identification of Possible Drug Treatment of Coronavirus Disease-19 (COVID-19) through Computational Drug Repurposing Study. J Chem Inf Model 60(6):3277–3286. https://doi.org/10.1021/acs.jcim.0c00179
43. Sharma P, Joshi T, Mathpal S, Joshi T, Pundir H, Chandra S, Tamta S (2020) Identification of natural inhibitors against Mpro of SARS-CoV-2 by molecular docking, molecular dynamics simulation, and MM/PBSA methods. J Biomol Struct Dyn. https://doi.org/10.1080/07391102.2020.1842806
44. Deeks HM, Walters RK, Barnoud J, Glowacki DR, Mulholland AJ (2020) Interactive Molecular Dynamics in Virtual Reality Is an Effective Tool for Flexible Substrate and Inhibitor Docking to the SARS-CoV-2 Main Protease. J Chem Inf Model 60(12):5803–5814. https://doi.org/10.1021/acs.jcim.0c01030
45. Liang J, Pitsillou E, Karagiannis C, Darmawan KK, Ng K, Hung A, Karagiannis TC (2020) Interaction of the prototypical α-ketoamide inhibitor with the SARS-CoV-2 main protease active site in silico: Molecular dynamic simulations highlight the stability of the ligand-protein complex. Comput Biol Chem 87:107292. https://doi.org/10.1016/j.compbiolchem.2020.107292
46. Keretsu S, Bhujbal SP, Cho SJ (2020) Rational approach toward COVID-19 main protease inhibitors via molecular docking, molecular dynamics simulation and free energy calculation. Sci Reports 10(1):17716. https://doi.org/10.1038/s41598-020-74468-0
47. Dallocchio RN, Dessì A, Vito AD, Delogu G, Andrea P, Madeddu G (2020) Early combination treatment with existing HIV antivirals: an effective treatment for COVID-19? Res Sq. https://doi.org/10.21203/rs.3.rs-35791/v1
48. Xue X, Yu H, Yang H, Xue F, Wu Z, Shen W, Li J, Zhou Z, Ding Y, Zhao Q, Zhang XC, Liao M, Bartlam M, Rao Z (2008) Structures of Two Coronavirus Main Proteases: Implications for Substrate Binding and Antiviral Drug Design. J Virol 82(5):2515–2527. https://doi.org/10.1128/JVI.02114-07
49. Goyal B, Goyal D (2020) Targeting the Dimerization of the Main Protease of Coronaviruses: A Potential Broad-Spectrum Therapeutic Strategy. ACS Comb Sci 22(6):297–305. https://doi.org/10.1021/acscombsci.0c00058
50. Nguyen D, Gao K, Chen J, Wang R, Wei G-W (2020) Unveiling the molecular mechanism of SARS-CoV-2 main protease inhibition from 92 crystal structures.
51. Srivastava V, Yadav A, Sarkar P (2020) Molecular docking and ADMET study of bioactive compounds of Glycyrrhiza glabra against main protease of SARS-CoV2. Materials Today, Proceedings. https://doi.org/10.1016/j.matpr.2020.10.055 (Advance online publication)
52. Yang H, Lou C, Sun L, Li J, Cai Y, Wang Z, Li W, Liu G, Tang Y (2019) admetSAR 2.0: web-service for prediction and optimization of chemical ADMET properties. Bioinformatics 35(6):1067–1069. https://doi.org/10.1093/bioinformatics/bty707
53. Ong W-Y, Go M-L, Wang D-Y, Cheah IK-M, Halliwell B (2020) Effects of antimalarial drugs on neuroinflammation-potential use for treatment of covid-19-related neurologic complications. Mol Neurobiol. https://doi.org/10.1007/s12035-020-02093-z
54. Lam S, Lombardi A, Ouanounou A (2020) COVID-19: a review of the proposed pharmacological treatments. Eur J Pharmacol 886:173451. https://doi.org/10.1016/j.ejphar.2020.173451
55. Li X, Höhl R, Sörgel F, Fuhr U (2020) The parent drugs chloroquine and hydroxychloroquine do not inhibit human CYP3A activity in vitro. Eur J Clin Pharmacol 76(10):1481–1482. https://doi.org/10.1007/s00228-020-02928-7
56. Projean D, Baune B, Farinotti R, Flinois JP, Beaune P, Taburet AM, Ducharme J (2003) In vitro metabolism of chloroquine: identification of CYP2C8, CYP3A4, and CYP2D6 as the main isoforms catalyzing N-desethylchloroquine formation. Drug Metab Dispos 31(6):748–754. https://doi.org/10.1124/dmd.31.6.748
57. White NJ, Watson JA, Hoglund RM, Chan XHS, Cheah PY, Tarning J (2020) COVID-19 prevention and treatment: a critical analysis of chloroquine and hydroxychloroquine clinical pharmacology. PLOS Med 17(9):e1003252. https://doi.org/10.1371/journal.pmed.1003252
58. Deng P, Zhong D, Yu K, Zhang Y, Wang T, Chen X (2013) Pharmacokinetics, metabolism, and excretion of the antiviral drug arbidol in humans. J Antimicrobial Agent Chemotherapy 57(4):1743–1755. https://doi.org/10.1128/AAC.02282-12
59. Lamb YN (2020) Remdesivir: first approval. Drugs 80(13):1355–1363. https://doi.org/10.1007/s40265-020-01378-w
60. Mansuri Z, Shah B, Zafar MK, Jolly T, Jain S (2020) Remdesivir and potential interactions with psychotropic medications: A COVID-19 perspective. Prim Care Companion CNS Disord 22 (3). doi: https://doi.org/10.4088/PCC.20com02664
61. Yang K (2020) What do we know about remdesivir drug interactions? Clin andTransl Sci 13(5):842–844. https://doi.org/10.1111/cts.12815
62. Mirjalili M, Shafiekhani M, Vazin A (2020) Coronavirus disease 2019 (COVID-19) and transplantation: pharmacotherapeutic management of immunosuppression regimen. Ther Clin Risk Manag 16:617–629. https://doi.org/10.2147/tcrm.S256246
63. Walker O, Birkett D, Alvan G, Gustafsson L, Sjoqvist F (1983) Characterization of chloroquine plasma protein binding in man. 15 (3):375-377. doi: https://doi.org/10.1111/j.1365-2125.1983.tb01513.x
64. Furst DE (1996) Pharmacokinetics of hydroxychloroquine and chloroquine during treatment of rheumatic diseases. Lupus 5(Suppl 1):S11-15
65. Warhurst DC, Steele JC, Adagu IS, Craig JC, Cullander C (2003) Hydroxychloroquine is much less active than chloroquine against chloroquine-resistant Plasmodium falciparum, in agreement with its physicochemical properties. J Antimicrob Chemother 52(2):188–193. https://doi.org/10.1093/jac/dkg319
66. Chaijamorn W, Rungkitwattanakul D, Nuchtavorn N, Charoensareerat T, Pattharachayakul S, Sirikun W, Srisawat N (2020) Antiviral dosing modification for coronavirus disease 2019–infected patients receiving extracorporeal therapy. Crit Care Explor 2(10):e0242. https://doi.org/10.1097/CCE.0000000000000242
67. Lipinski CA, Lombardo F, Dominy BW, Feeney PJ (1997) Experimental and computational approaches to estimate solubility and permeability in drug discovery and development settings. Adv Drug Deliv Rev 23(1):3–25. https://doi.org/10.1016/S0169-409X(96)00423-1